Title
Electrochemical Cycling of Redox-Active Boron Cluster-Based Materials in the Solid State

Journal
Journal of the American Chemical Society, 145(26)

ISSN
0002-7863 1520-5126

Authors
Ready, Austin D
Irshad, Ahamed
Kallistova, Anna
et al.

Publication Date
2023-06-23

DOI
10.1021/jacs.3c03065

Peer reviewed

Electrochemical Cycling of Redox-Active Boron Cluster-Based Materials in the Solid State

Austin D. Ready,[a†] Ahamed Irshad,[b†] Anna Kallistova,[c] Moises Carrillo,[a] Milan Gembicky,[e] Ram Seshadri,[c,d] Sri Narayan,[b] Alexander M. Spokoyny*[a,f]*

[a]Department of Chemistry and Biochemistry, University of California, Los Angeles, Los Angeles, CA 90095, USA

[b]Department of Chemistry and Loker Hydrocarbon Research Institute, University of Southern California, Los Angeles, CA 90089, USA

[c]Materials Department and Materials Research Laboratory, University of California, Santa Barbara, Santa Barbara, CA 93106, USA

[d]Department of Chemistry and Biochemistry, University of California, Santa Barbara, Santa Barbara, CA 93106, USA

[e]Department of Chemistry and Biochemistry, University of California, San Diego, La Jolla, CA 92521, USA

[f]California NanoSystems Institute (CNSI), University of California, Los Angeles, CA 90095, USA

[†]These authors contributed equally

ABSTRACT: This work demonstrates the first successful electrochemical cycling of a redox-active boron cluster-based material in the solid state. Specifically, we designed and synthesized an ether-functionalized dodecaborate cluster, $B_{12}(OCH_3)_{12}$, which is the smallest redox-active building block in the $B_{12}(OR)_{12}$ family. This species can reversibly access four oxidation states in solution, ranging from a dianion to a radical cation. We show that a chemically isolated and characterized neutral $[B_{12}(OCH_3)_{12}]^0$ cluster can be utilized as a cathode active material in a PEO-based rechargeable all-solid-state cell with a lithium metal anode. The cell exhibits an impressive active material utilization close to 95% at C/20 rate, a high Coulombic efficiency of 96%, and reversibility, with only 4% capacity fade after 16 days of cycling. This work represents a conceptual departure in the development of redox-active components for electrochemical storage and serves as an entry point to a broader class of borane-based materials.

INTRODUCTION: In the past several decades, many researchers have advanced our knowledge of how carbon-based organic redox-active molecules can be incorporated into solid state battery materials.[1-8] Through solubility modifications via molecular weight, the addition of hydrophobic/hydrophilic groups, or impregnation in porous/polymeric materials, a number of redox-active small molecules (e.g., carbonyls, nitroxides, imides, disulfides, etc.) have been observed to retain their solution-phase redox activity in the solid state. Despite these advances, the incorporation of other well-defined covalent-based systems into electrochemically active materials in the solid state has been fundamentally underexplored. For example, polyhedral boron clusters, which are often described as three-dimensional aromatic analogues of benzene, can exhibit well-defined redox properties in solution, as seen for boranes ($[B_nH_n]^{2-}$; $n \leq 12$), carboranes, and their numerous functionalized derivatives.[9-45] Historically, a number of boron-based clusters have been deemed redox-inert species with wide electrochemical stability windows, prompting early studies of $Li_2B_{12}Cl_{12}$ and $Li_2B_{10}Cl_{10}$ as novel electrolytes, first in $SOCl_2$[23, 46] and later in ethereal solvents.[47-49] More recently, there have been extensive efforts in developing some of these clusters for solid state electrolyte applications.[50-87]

Recent advances in boron cluster chemistry[44-45, 88-98] show that judicious exopolyhedral modifications of these species can result in the emergence of boron-centered redox events in solution, which in many cases can be tunable. In particular, ether-functionalized dodecaborate clusters [$B_{12}(OR)_{12}$; R = alkyl, aryl] demonstrate the richest solution-based redox behavior exhibited by boron clusters studied to date.[14, 95-97, 99-112] Due to the enhanced electronic stabilization provided by the ether groups, the majority of these boron clusters have access to four stable oxidation states in solution (Figure 1A). Their redox potentials can be tuned over a wide voltage range through simple modification of the electron-donating or withdrawing nature of the carbon-based substituent (Figure 1B). Specifically, our research group has studied these clusters as redox-active polymer dopants,[113-114] photooxidants,[103, 111] and electroactive species for redox-flow batteries.[108] Surprisingly, however, there have been no reports so far demonstrating that boron clusters in general have the ability to undergo redox processes in the solid state.

Due to their robustness[59-60, 115] and chemical tunability, polyhedral boron clusters present a potentially appealing platform for translating solution-phase redox behavior into solids. In this work, we describe for the first time the development of a model boron cluster-based system that can undergo reversible redox in the solid state. As a result, we show the successful incorporation of redox-active $B_{12}(OCH_3)_{12}$ into an electrochemical cell to demonstrate the feasibility of boron clusters for energy storage applications (Figure 1C).

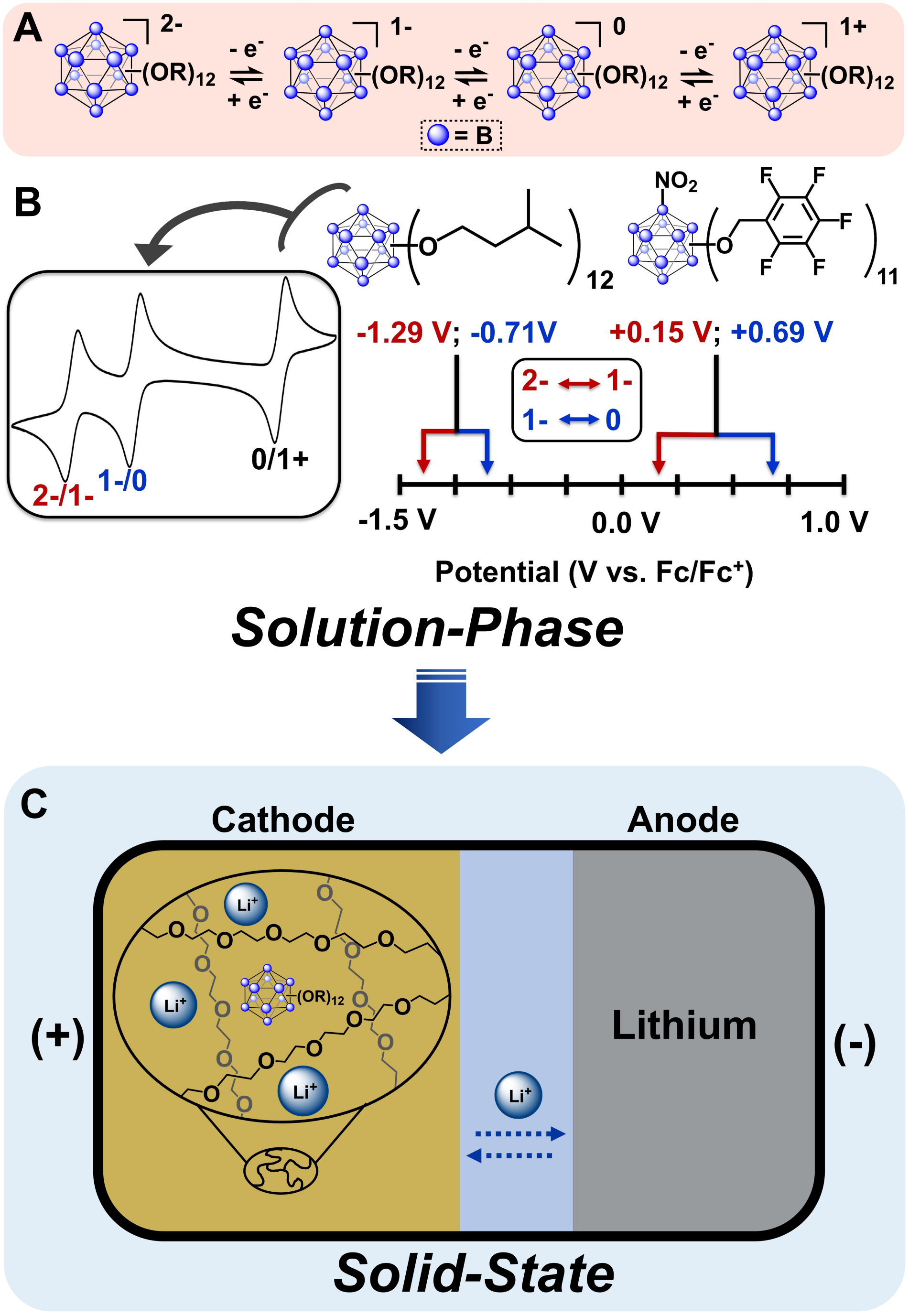

Figure 1. (A) Known reversible electronic transitions of $B_{12}(OR)_{12}$ clusters (B) Redox potentials of two representative $B_{12}(OR)_{12}$ clusters; cyclic voltammogram of B_{12}(O-3-methylbutyl)$_{12}$ (inset) (C) Depiction of a solid state electrochemical cell containing $B_{12}(OR)_{12}$ in a PEO matrix.

RESULTS & DISCUSSION: From a chemical design perspective, the ideal redox-active $B_{12}(OR)_{12}$ building block for electrochemical storage requires access to reversible, multi-electron redox, as well as a low molecular weight to ensure sufficient specific capacity. Furthermore, we hypothesize that in order to facilitate lithiation/delithiation, the oxygen atoms on the OR groups of the $B_{12}(OR)_{12}$ species should be sterically accessible to allow reversible metal ion coordination. All of these criteria exclude the previously developed alkylated and benzylated $B_{12}(OR)_{12}$ clusters studied thus far.

We hypothesized that the $B_{12}(OCH_3)_{12}$ cluster would serve as an ideal synthetic target for potential incorporation into a redox-active solid state material. Hawthorne and coworkers have previously reported the synthesis of this cluster[99] using a high-pressure reactor, starting from the tetrabutylammonium (TBA) salt of $[B_{12}(OH)_{12}]^{2-}$ and a large excess of methyl tosylate as a methylating agent. Importantly, the use of super stoichiometric amounts of methyl tosylate renders the purification of the final product cumbersome and reduces its overall purity. As such, we established a new facile microwave-assisted method to synthesize $B_{12}(OCH_3)_{12}$ (Figure 2A) using trimethylsulfoxonium bromide (TMSO-Br), which does not produce difficult to remove byproducts, allowing the cluster to be easily isolated. In a typical reaction, 60 mg of $TBA_2B_{12}(OH)_{12}$ is stirred with Hünig's base and 100 equivalents of TMSO-Br in air for 1 hour at 120°C in a microwave reactor, producing perfunctionalized $[B_{12}(OCH_3)_{12}]^{2-/1-}$, as judged by in situ ^{11}B NMR spectroscopy and mass spectrometry (SI, Figure S1-S4). Full methoxylation of all twelve boron vertices is confirmed when numerous peaks in the ^{11}B NMR spectrum (indicating partial substitution/desymmetrization of the cluster) coalesce to a broad singlet at -17 ppm.

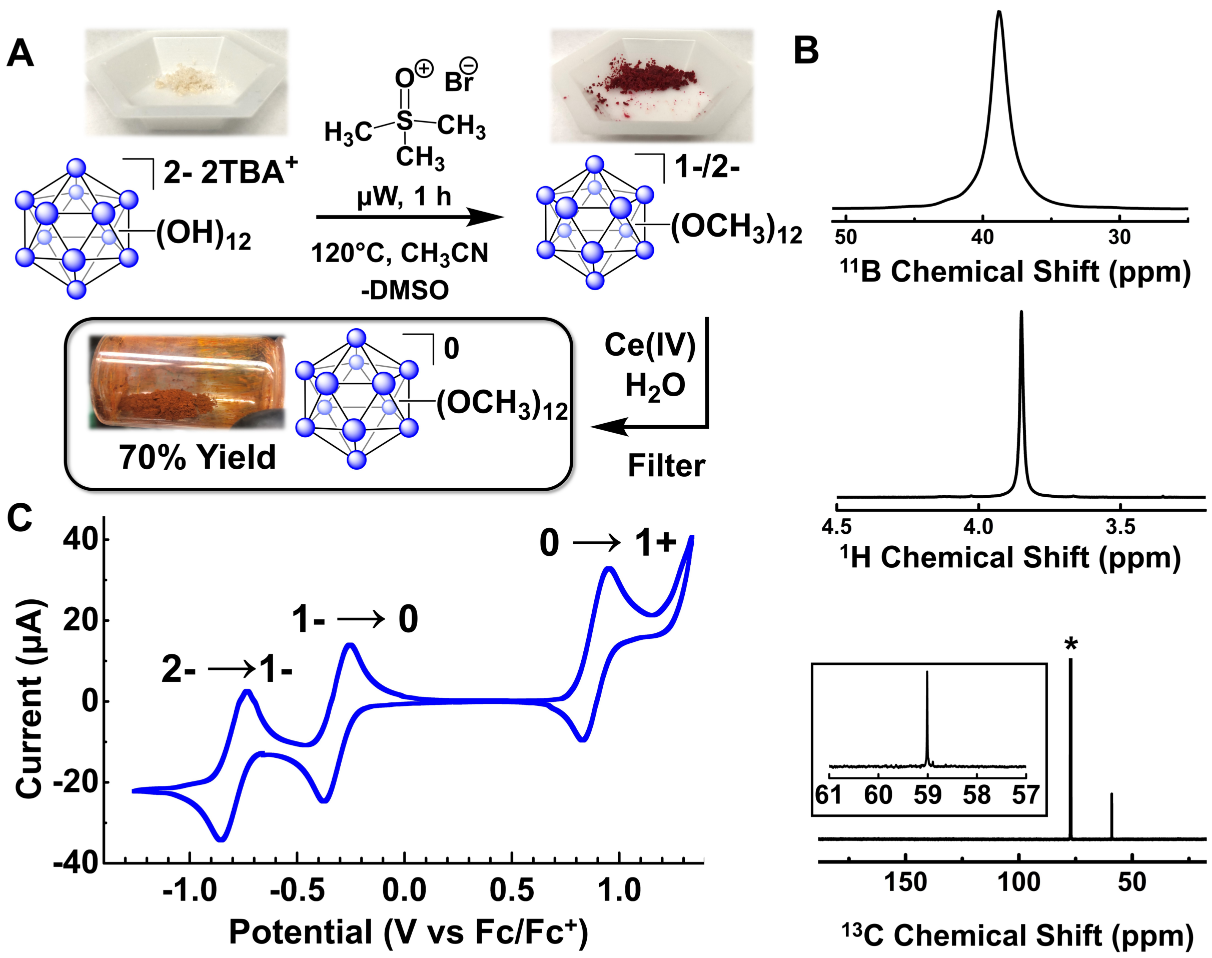

Figure 2. (A) Microwave-assisted synthesis of $[B_{12}(OCH_3)_{12}]^{1-/2-}$, followed by chemical oxidation. (B) ^{11}B, ^{1}H, and ^{13}C NMR spectra, respectively, of $[B_{12}(OCH_3)_{12}]^0$ in $CDCl_3$ (asterisk represents solvent) (C) Cyclic voltammogram of $B_{12}(OCH_3)_{12}$ in DCM.

Upon mixing $[B_{12}(OCH_3)_{12}]^{2-/1-}$ with an aqueous solution of Ce(IV), the original ^{11}B NMR signal at -17 ppm disappears, with a concomitant emergence of a new signal at 38 ppm (Figure 2B), consistent with the formation of a neutral $B_{12}(OCH_3)_{12}$ species, which immediately precipitates as an orange solid. This material is then subjected to a simple purification via filtration and solvent washes. The complete removal of cerium salts is confirmed by XPS (SI, Figure S18) and electrochemical characterization of the resulting product (Figure 2C). The chemical structure and oxidation state assignment of $B_{12}(OCH_3)_{12}$ were confirmed through multiple characterization methods, including solution-phase NMR spectroscopy (^{11}B, ^{13}C, ^{1}H) (Figure 2B), mass spectrometry (SI, Figure S1 and S2), and single crystal and powder X-ray crystallography (Figure 3). The high symmetry of the dodecaborate cluster is exemplified by the single resonance observed via ^{11}B, ^{13}C, and ^{1}H NMR spectroscopy (Figure 2B; SI, Figure S3-S6). As determined from the single crystal structure, $B_{12}(OCH_3)_{12}$ crystallizes in a trigonal $R\bar{3}$ space group. Considering that the single crystal measurements were collected at 100 K, we performed additional X-ray diffraction measurements on powder samples at room temperature in order to elucidate structural features under more relevant ambient conditions. An *ab initio* structure solution was obtained via Rietveld refinement of experimental powder data of $B_{12}(OCH_3)_{12}$. Temperature has a significant effect on the unit cell of $B_{12}(OCH_3)_{12}$, as evident by the 0.6% lattice expansion when comparing the structure as determined from powder data (295 K) versus single crystal data (100 K). Despite this, the structure determined via refinement of the powder data shows excellent agreement with the single crystal structure (Figure 3; SI, Figure S30 and Table S1-S8). In the single crystal data, the cluster shows average bond distances of 1.85 Å (B-B), 1.39 Å (B-O), and 1.42 Å (O-C), in line with observed bond distances for other $B_{12}(OR)_{12}$ clusters[96-97, 104] and simulated values[116] for neutral $B_{12}(OCH_3)_{12}$.

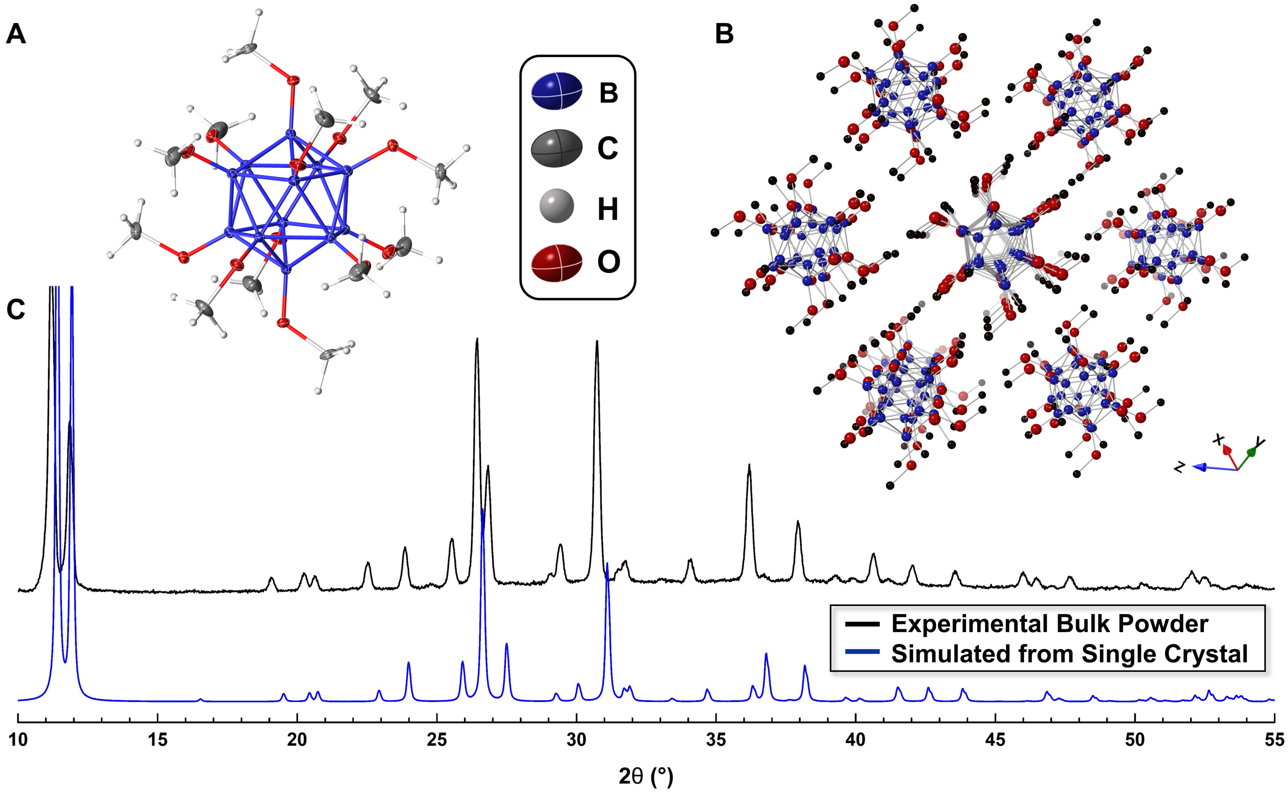

Figure 3. (A) Single crystal structure of $B_{12}(OCH_3)_{12}$ (non-hydrogen atoms depicted as 50% probability ellipsoids; hydrogens depicted as spheres) (B) Extended packing of boron clusters (hydrogens omitted for clarity). (C) Simulated and experimental powder diffraction patterns of $B_{12}(OCH_3)_{12}$.

The packing motif of $B_{12}(OCH_3)_{12}$ as a powder (Figure 3B) shows ample interstitial space (~3 Å cavities between clusters; SI, Figure S32), suggesting the possibility of metal ion insertion. Furthermore, this cluster also shows access to multiple oxidation states in solution (Figure 2C), as well as a radical cationic state, a phenomenon recently observed[102, 107] by our group for many other $B_{12}(OR)_{12}$ clusters. $B_{12}(OCH_3)_{12}$ shows redox activity over a wide voltage window in solution, with half-wave potentials ($E_{1/2}$) spanning a range of more than 1 V, from -0.79 V vs Fc/Fc$^+$ (2- → 1-) up to +0.89 V (0 → 1+), in good agreement with previous observations of the effect of the R substituent on the redox potentials of $B_{12}(OR)_{12}$ clusters.[96-97, 102, 107] Elucidation of the atomic-level structure of $B_{12}(OCH_3)_{12}$, in combination with the rich redox behavior in solution, further prompted us to test our original hypothesis and explore whether this material would be a viable candidate for a solid state electrochemical cell.

A model solid state Li-ion cell was constructed with $B_{12}(OCH_3)_{12}$ as the active cathode material (see SI for details), and cyclic voltammetry of the $B_{12}(OCH_3)_{12}$/PEO-SPE/Li cell was performed (Figure 4A). PEO was chosen as the solid electrolyte owing to its high Li-ion conductivity at moderate temperature, flexibility, easy cell fabrication, excellent chemical stability, and high electrochemical stability in the potential window of interest. The cell was first subjected to a cathodic scan starting from its open circuit potential (OCP) of 3.4 V to 1.5 V, followed by an anodic sweep to 4.15 V. The lower and upper voltage limits were chosen to avoid contributions from lithium intercalation into carbon and oxidative decomposition of PEO, respectively. During the cathodic sweep (Figure 4A), significant Faradaic current flow started around 3.40 V to form a broad reduction peak centered around 3.30 V. During the anodic sweep, the corresponding oxidation peak appeared at 3.60 V. Thus, the half wave potential is roughly 3.45 V vs. Li^+/Li, in excellent agreement with the expected value for the $[B_{12}(OCH_3)_{12}]^0/[B_{12}(OCH_3)_{12}]^{1-}$ redox couple, suggesting successful lithiation and delithiation (SI, Figure S27).

The phenomenon suggested by this data is unprecedented for boron clusters in the solid state. Namely, that Li-ions can reversibly intercalate into the cathode during discharge, reducing neutral $B_{12}(OCH_3)_{12}$ clusters to their monoanionic state, followed by a reversal of this process during charging. $E_{1/2}$ remained the same in the subsequent cycles, although a gradual increase of the peak current in the first few cycles was noted. This data suggested a steady increase in the utilization of the active material with cycling due to a gradual wetting of the electrode with the polymer electrolyte, as observed in PEO-based solid state cells.[117-118] Additionally, the ratio of integrated charge under the reduction and oxidation peaks (i.e., Coulombic efficiency) increased from 78% to 95%. The lower efficiency in the initial cycle can be attributed to the formation of a solid electrolyte interface (SEI) on both the positive and negative electrodes. Once a stable SEI was formed, however, a remarkable Coulombic efficiency of 95% was achieved, signifying highly reversible redox behavior of the boron cluster in the solid state, a crucial prerequisite for use as a battery-active material.

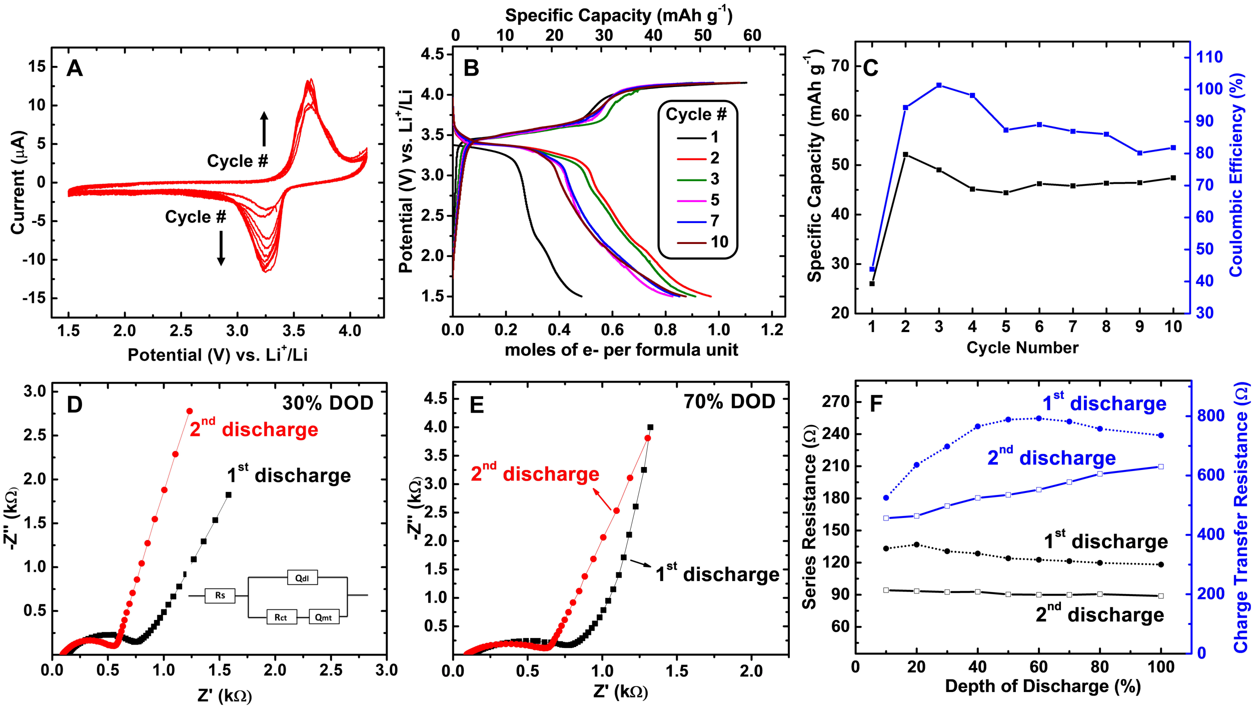

Figure 4. (A) Cyclic voltammetry of a $B_{12}(OCH_3)_{12}$/PEO-SPE/Li cell at 0.1 mV s^{-1}. (B) Galvanostatic cycling at C/20 rate. (C) Variation in specific capacity and Coulombic efficiency with cycle number. (D) Nyquist plots at 30% DOD and (E) 70% DOD. (F) Variation in series and charge transfer resistances with DOD during the first two discharge steps. All measurements were performed at 60°C.

To further demonstrate the utility of this boron cluster for solid state battery applications, galvanostatic cycling was carried out at a C/20 rate (C-rate is based on 1 e^- transfer per formula unit). The specific capacity based on a 1 e- redox process was 53 mAh g^{-1}. Although only 50% of the theoretical capacity was obtained in the first discharge, a theoretical capacity of 95% and a high coulombic efficiency of 96% were observed in the second cycle (Figure 4B and 4C), consistent with the gradual rise of peak current observed during cyclic voltammetry (Figure 4A). The cell also showed high cycling stability, retaining 48 mAh g^{-1} even after ~16 days of cycling (10 cycles at C/20 rate). Measurements were also performed at numerous C-rates and for more cycles (SI, Figure S25 and S26). The charge and discharge curves maintained similar voltage plateaus and sloped regions in all cycles, indicating similar reaction pathways throughout the cycling. Post-mortem XPS of a discharged cell suggests the presence of intact $B_{12}(OCH_3)_{12}$-based clusters in a reduced oxidation state (SI, Figure S24). Unlike traditional all-solid-state cells, which often show significant capacity decay in the first few cycles,[119] the high interfacial stability and intimate contact between the boron cluster electrode and the flexible polymer solid electrolyte is primarily responsible for the remarkable reversibility and capacity retention.

Electrochemical impedance spectroscopy (EIS) was carried out at different depths of discharge (DOD) during the first and second discharge steps to probe the variation in the internal resistance of the cell during cycling. Nyquist plots in the range of 100 kHz to 0.1 Hz show a depressed semicircle at high to medium frequency and an inclined line in the low frequency region (Figure 4D and 4E). The diameter of the semicircle is smaller in the second discharge at both 30% and 70% DOD, indicating a lowered resistance for the charge transfer process at the electrode/electrolyte interface. We also modeled the Nyquist plots using an equivalent circuit, $R_s(Q_{dl}(R_{ct}Q_{mt}))$ where R_s is series resistance, R_{ct} is charge transfer resistance, Q_{dl} and Q_{mt} are the constant phase elements representing double layer capacitance and mass transfer process, respectively (Figure 4D, inset). The constant phase element (Q) substituted an ideal capacitor (C), in consideration of the distributed capacitive elements of the porous electrode.[120] The series resistance (R_s) included the sum of resistance contributions from the electrolyte, current collectors, and electrodes. $R_s = \sim 120\ \Omega$ at all values of DOD in the first discharge and is reduced to ~90 Ω in the second discharge (Figure 4F). This decrease in R_s with cycle number indicates improved interfacial contact and electrode wetting during cycling.[117-118] Similarly, the charge transfer resistance (R_{ct}) at all levels of lithiation in the second cycle is lower than that of the first cycle. For instance, at 50% DOD, $R_{ct} = 800\ \Omega$ in the first discharge, whereas it is only 550 Ω in the second cycle (Figure 4F). The lower values of both R_s and R_{ct} in the second cycle reduce the overall internal resistance of the cell, leading to better utilization of the electrode and higher capacity.

In order to probe the structure and electrochemistry of the lithiated boron cluster, which was presumably formed during cycling as an electrochemically derived intermediate, we independently synthesized the reduced cluster in the dianionic state with a lithium cation, $Li_2[B_{12}(OCH_3)_{12}]$, and tested it in an identical electrochemical cell (see SI for details). The lithiated cluster was synthesized in good yield through a simple reduction of the neutral cluster in solution with methyl lithium, which proceeded to the fully reduced dianionic cluster. Solution-phase ^{11}B, ^{1}H, and ^{7}Li NMR confirmed the presence of $[B_{12}(OCH_3)_{12}]^{2-}$ with lithium cations (SI, Figure S11-13). Additionally, the reduction of the cluster from 0 to 2- could be observed via X-ray photoelectron spectroscopy (XPS) as a decrease of 1.0 eV in the binding energy of boron 1s electrons (SI, Figure S22), in excellent agreement with our previous observations of an ~0.5 eV shift per each one electron reduction of $B_{12}(OR)_{12}$.[97, 107] Unfortunately, the cell containing $Li_2[B_{12}(OCH_3)_{12}]$ showed inferior electrochemical performance compared to that using neutral

$B_{12}(OCH_3)_{12}$ (Figure S28). Attempts were made to refine the synchrotron data of $Li_2[B_{12}(OCH_3)_{12}]$, but a $LiOH{\cdot}H_2O$ impurity phase was identified which precluded thorough analysis (SI, Figure S31). There are a number of potential reasons for the observed poor solid state cycling behavior and large voltage hysteresis when the chemically lithiated cluster is used as a cathode material. It is anticipated that the presence of the ionically and electronically insulating impurity phase could reduce the overall crystallinity, as well as impede the electron and Li-ion mobility in the lattice, leading to poor electrochemical performance.

CONCLUSION: We have demonstrated the first example of a boron cluster undergoing reversible redox processes in the solid state. Through careful consideration of desirable properties, including low molecular weight, multiple redox events, and sterically accessible ether groups, a methoxy-functionalized boron cluster—$B_{12}(OCH_3)$—was identified as an ideal candidate and synthesized using a microwave reactor. After observing electrochemical behavior in solution, this cluster was then incorporated into an all-solid-state Li-ion cell with a PEO solid electrolyte. The cell could be cycled to utilize 95% of the active material at C/20 rate, with high Coulombic efficiency of 96% and reversibility, retaining 96% of the initial capacity even after 16 days of cycling. Overall, this work represents an important departure from the status quo in cathode material design, opening up a new class of materials for this application. Further improvements for this class of materials can be achieved either by incorporating redox-active cations[121] or reducing the molecular weight of the cluster through the use of smaller polyhedral borane cores.[13, 15, 19, 38] The continued success of this approach will rely on further reducing the molecular weight of the redox-active boron clusters, as well as developing well-defined design rules that govern the interactions between the redox-active anions and cations.

ASSOCIATED CONTENT

Supporting Information

The Supporting Information is available free of charge at https://pubs.acs.org/doi/xxxxx.

General information, synthetic procedures, and characterization data (PDF)

$B_{12}(OCH_3)_{12}$ crystallographic information file (CIF) and checkCIF (PDF)

Crystallographic data are available from the Cambridge Crystallographic Data Centre, under the reference number: CCDC 2239297

AUTHOR INFORMATION

Corresponding Authors

*E-mail: spokoyny@chem.ucla.edu; srnaraya@usc.edu

Author Contributions

The manuscript was written through contributions of all authors. All authors have given approval to the final version of the manuscript.

ACKNOWLEDGMENTS

This work was supported as part of the Center for Synthetic Control Across Length Scales for Advancing Rechargeables (SCALAR), an Energy Frontier Research Center funded by the U.S. Department of Energy, Office of Science, Basic Energy Sciences under Award DE-SC0019381.

The research reported here made use of shared facilities of the UC Santa Barbara Materials Research Science and Engineering Center (MRSEC, NSF DMR 1720256), a member of the Materials Research Facilities Network (http://www.mrfn.org) and the Advanced Photon Source at Argonne National Laboratory, which was supported by the U. S. Department of Energy, Office of Science, Office of Basic Energy Sciences, under Contract No. DE-AC02-06CH11357. A. M.S. thanks NSF Grant CHE-1846849 (NSF CAREER Award) and the Dreyfus Foundation for the Camille Dreyfus Teacher-Scholar Award for additional support. Authors thank Dr. Ignacio Martini for assistance with XPS and Ms. Yessica Nelson for assistance with NMR spectroscopy.

REFERENCES

(1) Gannett, C. N.; Melecio-Zambrano, L.; Theibault, M. J., et al., Organic electrode materials for fast-rate, high-power battery applications. *Materials Reports: Energy,* **2021,** *1* (1), 100008.

(2) Liang, Y.; Tao, Z.; Chen, J., Organic Electrode Materials for Rechargeable Lithium Batteries. *Adv. Energy Mater.,* **2012,** *2* (7), 742-769.

(3) Liang, Y.; Yao, Y., Positioning Organic Electrode Materials in the Battery Landscape. *Joule,* **2018,** *2* (9), 1690-1706.

(4) Lyu, H.; Sun, X.-G.; Dai, S., Organic Cathode Materials for Lithium-Ion Batteries: Past, Present, and Future. *Adv. Energy Sustainability Res.,* **2021,** *2* (1), 2000044.

(5) Muench, S.; Wild, A.; Friebe, C., et al., Polymer-Based Organic Batteries. *Chem. Rev.,* **2016,** *116* (16), 9438-9484.

(6) Schon, T. B.; McAllister, B. T.; Li, P.-F.; Seferos, D. S., The rise of organic electrode materials for energy storage. *Chem. Soc. Rev.,* **2016,** *45* (22), 6345-6404.

(7) Song, Z.; Zhou, H., Towards sustainable and versatile energy storage devices: an overview of organic electrode materials. *Energy & Environmental Science,* **2013,** *6* (8), 2280-2301.

(8) Xie, J.; Zhang, Q., Recent Progress in Multivalent Metal (Mg, Zn, Ca, and Al) and Metal-Ion Rechargeable Batteries with Organic Materials as Promising Electrodes. *Small,* **2019,** *15* (15), 1805061.

(9) Núñez, R.; Tarrés, M.; Ferrer-Ugalde, A., et al., Electrochemistry and Photoluminescence of Icosahedral Carboranes, Boranes, Metallacarboranes, and Their Derivatives. *Chem. Rev.,* **2016,** *116* (23), 14307-14378.

(10) Morris, J. H.; Gysling, H. J.; Reed, D., Electrochemistry of boron compounds. *Chem. Rev.,* **1985,** *85* (1), 51-76.

(11) Grimes, R. N. *Carboranes*. 2 ed.; Academic Press, 2011, pp 985-1019.

(12) Pospíšil, L. r.; King, B. T.; Michl, J., Voltammetry in benzene using lithium dodecamethylcarba-closo-dodecaborate, $LiCB_{11}Me_{12}$, as a supporting electrolyte: reduction of Ag^+. *Electrochim. Acta,* **1998,** *44* (1), 103-108.

(13) Axtell, J. C.; Kirlikovali, K. O.; Jung, D., et al., Metal-Free Peralkylation of the closo-Hexaborate Anion. *Organometallics,* **2017,** *36* (6), 1204-1210.

(14) Axtell, J. C.; Saleh, L. M. A.; Qian, E. A., et al., Synthesis and Applications of Perfunctionalized Boron Clusters. *Inorg. Chem.,* **2018,** *57* (5), 2333-2350.

(15) Bykov, A. Y.; Zhdanov, A. P.; Zhizhin, K. Y.; Kuznetsov, N. T., Structure, physicochemical properties, and reactivity of the $[B_9H_9]^{2-}$ anion. *Russ. J. Inorg. Chem.,* **2016,** *61* (13), 1629-1648.

(16) Peymann, T.; Knobler, C. B.; Khan, S. I.; Hawthorne, M. F., Dodecamethyl-closo-dodecaborate(2−). *Inorg. Chem.,* **2001,** *40* (6), 1291-1294.

(17) Preetz, W.; Peters, G., The Hexahydro-closo-hexaborate Dianion $[B_6H_6]^{2-}$ and Its Derivatives. *Eur. J. Inorg. Chem.,* **1999,** *1999* (11), 1831-1846.

(18) Ivanov, S. V.; Miller, S. M.; Anderson, O. P., et al., Synthesis and Stability of Reactive Salts of Dodecafluoro-closo-dodecaborate(2−). *J. Am. Chem. Soc.,* **2003,** *125* (16), 4694-4695.

(19) Li, X.; Yang, T.; Zhou, J., Synergetic ligand and size effects of boron cage based electrolytes in Li-ion batteries. *Phys. Chem. Chem. Phys.,* **2022,** *24* (18), 11345-11352.

(20) Hawthorne, M. F.; Shelly, K.; Li, F., The versatile chemistry of the $[B_{20}H_{18}]^{2-}$ ions: novel reactions and structural motifs. *Chem. Commun.,* **2002,** (6), 547-554.

(21) Wahab, A.; Stepp, B.; Douvris, C., et al., Measured and Calculated Oxidation Potentials of 1-X-12-Y-$CB_{11}Me_{10}^{-}$ Anions. *Inorg. Chem.,* **2012,** *51* (9), 5128-5137.

(22) Ivanov, S.; Casteel, W.; Pez, G.; Ulman, M. Polyfluorinated boron cluster anions for lithium electrolytes. US 20050064288A1, 2005.

(23) Schlaikjer, C. R. Electrochemical cell with clovoborate salt in electrolyte and method of operation and composition of matter. 4,020,240, 1975.

(24) Wiersema, R. J.; Middaugh, R. L., Electrochemical preparation and halogenation of 1,1'-μ-hydro-bis(undecahydro-closo-dodecaborate)(3-), $B_{24}H_{23}^{3-}$. *Inorg. Chem.,* **1969,** *8* (10), 2074-2079.

(25) Bowden, W., Electrochemical Oxidation of Polyhedral Boron Halide Anions. *J. Electrochem. Soc.,* **1982,** *129* (6), 1249.

(26) Wiersema, R.; Middaugh, R. L., Electrochemical oxidation of $B_{12}H_{12}^{2-}$. *J. Am. Chem. Soc.,* **1967,** *89* (19), 5078-5078.

(27) Middaugh, R.; Farha Jr, F., Kinetics of Electrochemical Oxidative Coupling of Decahydroclovodecaborate (2-) in Acetonitrile. *J. Am. Chem. Soc.,* **1966,** *88* (18), 4147-4149.

(28) Zhang, J.; Fu, X.; Lin, Z.; Xie, Z., Supercarborane Radical Anions with 2n + 3 Electron Counts: A Combined Experimental and Theoretical Study. *Inorg. Chem.,* **2015,** *54* (4), 1965-1973.

(29) Kaczmarczyk, A.; Kolski, G. B.; Townsend, W. P., Oxidative Degradation of Polyhedral Boranes. *J. Am. Chem. Soc.,* **1965,** *87* (6), 1413-1413.

(30) Klanberg, F.; Eaton, D. R.; Guggenberger, L. J.; Muetterties, E. L., Chemistry of boranes. XXVIII. New polyhedral borane anions, $B_8H_8^{2-}$, $B_8H_8^{-}$, and $B_7H_7^{2-}$. *Inorg. Chem.,* **1967,** *6* (7), 1271-1281.

(31) Boeré, R. T.; Kacprzak, S.; Keßler, M., et al., Oxidation of closo-$[B_{12}Cl_{12}]^{2-}$ to the Radical Anion $[B_{12}Cl_{12}]^{-}$ and to Neutral $B_{12}Cl_{12}$. *Angew. Chem. Int. Ed.,* **2011,** *50* (2), 549-552.

(32) Lee, T. B.; McKee, M. L., Redox Energetics of Hypercloso Boron Hydrides B_nH_n (n = 6–13) and $B_{12}X_{12}$ (X = F, Cl, OH, and CH_3). *Inorg. Chem.,* **2012,** *51* (7), 4205-4214.

(33) Jelliss, P. A.; Mason, J.; Nazzoli, J. M., et al., Synthesis and Characterization of Ruthenacarborane Complexes Incorporating Chelating N-Donor Ligands: Unexpected Luminescence from the Complex $[3\text{-CO-}3,3\text{-}\{\kappa^2\text{-}Me_2N(CH_2)_2NMe_2\}\text{-closo-}3,1,2\text{-}RuC_2B_9H_{11}]$. *Inorg. Chem.,* **2006,** *45* (1), 370-385.

(34) Wiersema, R. J.; Hawthorne, M. F., Electrochemistry and boron-11 nuclear magnetic resonance spectra of monocarbon carboranes. *Inorg. Chem.,* **1973,** *12* (4), 785-788.

(35) Speiser, B.; Tittel, C.; Einholz, W.; Schäfer, R., Redox reactions of the boron subhalide clusters $B_nCl_n^{0/-/2-}$ (n = 8 or 9) investigated by electrochemical and spectroscopic methods. *J. Chem. Soc., Dalton Trans.,* **1999,** (11), 1741-1752.

(36) Speiser, B.; Wizemann, T.; Würde, M., Two-Electron-Transfer Redox Systems, Part 7: Two-Step Electrochemical Oxidation of the Boron Subhalide Cluster Dianions (X = Cl, Br, I). *Inorg. Chem.,* **2003,** *42* (13), 4018-4028.

(37) Einholz, W.; Vaas, K.; Wieloch, C., et al., Chemische und cyclovoltammetrische Untersuchung der Redoxreaktionen der Decahalogendecaborate closo-$[B_{10}X_{10}]^{2-}$ und hypercloso-$[B_{10}X_{10}]^{\cdot -}$ (X=Cl, Br). Kristallstrukturanalyse von $Cs_2[B_{10}Br_{10}]\cdot 2H_2O$. *Zeitschrift für anorganische und allgemeine Chemie,* **2002,** *628* (1), 258-268.

(38) Guschlbauer, J.; Shaughnessy, K. H.; Pietrzak, A., et al., $[\text{closo-}B_{10}H_8\text{-}1,10\text{-}(CN)_2]^{2-}$ as a Conduit of Electronic Effects: Comparative Studies of Fe⋯Fe Communication in $[\{(\eta^5\text{-}Cp)(dppe)Fe\}_2\{\mu^2\text{-}(NC\text{-}X\text{-}CN)\}]^{n+}$ (n = 0, 2). *Organometallics,* **2021,** *40* (15), 2504-2515.

(39) Ringstrand, B.; Kaszynski, P.; Young, V. G., Jr.; Janoušek, Z., Anionic Amino Acid $[\text{closo-}1\text{-}CB_9H_8\text{-}1\text{-}COO\text{-}10\text{-}NH_3]^{-}$ and Dinitrogen Acid $[\text{closo-}1\text{-}CB_9H_8\text{-}1\text{-}COOH\text{-}10\text{-}N_2]$ as Key

Precursors to Advanced Materials: Synthesis and Reactivity. *Inorg. Chem.,* **2010,** *49* (3), 1166-1179.

(40) Wedge, T. J.; Herzog, A.; Huertas, R., et al., Metal−Metal Communication through Carborane Cages Supporting Electroactive $[\eta^5\text{-CpFe(CO)}_2]$ Substituents. *Organometallics,* **2004,** *23* (3), 482-489.

(41) Fabre, B.; Clark, J. C.; Vicente, M. G. H., Synthesis and Electrochemistry of Carboranylpyrroles. Toward the Preparation of Electrochemically and Thermally Resistant Conjugated Polymers. *Macromolecules,* **2006,** *39* (1), 112-119.

(42) Mercer, G. D.; Lang, J.; Reed, R.; Scholer, F. R., Electrolytic Reduction of B-Oxy Derivatives of 2,3-Dicarba-closo-undecaborane(11). *Inorg. Chem.,* **1975,** *14* (4), 761-763.

(43) Teixidor, F.; Pedrajas, J.; Vinas, C., Cathodic Cleavage of CS and CP in Carboranyl Derivatives. *Inorg. Chem.,* **1995,** *34*, 1726-1729.

(44) King, B. T.; Körbe, S.; Schreiber, P. J., et al., The Sixteen $CB_{11}H_nMe_{12-n}^-$ Anions with Fivefold Substitution Symmetry: Anodic Oxidation and Electronic Structure. *J. Am. Chem. Soc.,* **2007,** *129* (43), 12960-12980.

(45) Malischewski, M.; Bukovsky, E. V.; Strauss, S. H.; Seppelt, K., Jahn–Teller Effect in the $B_{12}F_{12}$ Radical Anion and Energetic Preference of an Octahedral $B_6(BF_2)_6$ Cluster Structure over an Icosahedral Structure for the Elusive Neutral $B_{12}F_{12}$. *Inorg. Chem.,* **2015,** *54* (23), 11563-11566.

(46) Dey, A. N.; Miller, J., Primary Li / $SOCl_2$ Cells: VII . Effect of and Electrolyte Salts on the Performance. *J. Electrochem. Soc.,* **1979,** *126* (9), 1445.

(47) Johnson, J. W.; Brody, J. F., Lithium Closoborane Electrolytes: III . Preparation and Characterization. *J. Electrochem. Soc.,* **1982,** *129* (10), 2213.

(48) Johnson, J. W.; Whittingham, M. S., Lithium Closoboranes as Electrolytes in Solid Cathode Lithium Cells. *J. Electrochem. Soc.,* **1980,** *127* (7), 1653.

(49) Johnson, J. W.; Thompson, A. H., Lithium Closoboranes II . Stable Nonaqueous Electrolytes for Elevated Temperature Lithium Cells. *J. Electrochem. Soc.,* **1981,** *128* (4), 932.

(50) McArthur, S. G.; Jay, R.; Geng, L., et al., Below the 12-vertex: 10-vertex carborane anions as non-corrosive, halide free, electrolytes for rechargeable Mg batteries. *Chem. Commun.,* **2017,** *53* (32), 4453-4456.

(51) Sadikin, Y.; Brighi, M.; Schouwink, P.; Černý, R., Superionic Conduction of Sodium and Lithium in Anion-Mixed Hydroborates $Na_3BH_4B_{12}H_{12}$ and $(Li_{0.7}Na_{0.3})_3BH_4B_{12}H_{12}$. *Adv. Energy Mater.,* **2015,** *5* (21), 1501016.

(52) Tang, W. S.; Unemoto, A.; Zhou, W., et al., Unparalleled lithium and sodium superionic conduction in solid electrolytes with large monovalent cage-like anions. *Energy & Environmental Science,* **2015,** *8* (12), 3637-3645.

(53) Teprovich, J. A.; Colón-Mercado, H.; Washington Ii, A. L., et al., Bi-functional $Li_2B_{12}H_{12}$ for energy storage and conversion applications: solid-state electrolyte and luminescent down-conversion dye. *J. Mater. Chem. A,* **2015,** *3* (45), 22853-22859.

(54) Tutusaus, O.; Mohtadi, R.; Arthur, T. S., et al., An Efficient Halogen-Free Electrolyte for Use in Rechargeable Magnesium Batteries. *Angew. Chem. Int. Ed.,* **2015,** *54* (27), 7900-7904.

(55) Udovic, T. J.; Matsuo, M.; Tang, W. S., et al., Exceptional Superionic Conductivity in Disordered Sodium Decahydro-closo-decaborate. *Adv. Mater.,* **2014,** *26* (45), 7622-7626.

(56) Udovic, T. J.; Matsuo, M.; Unemoto, A., et al., Sodium superionic conduction in $Na_2B_{12}H_{12}$. *Chem. Commun.,* **2014,** *50* (28), 3750-3752.

(57) He, L.; Li, H.-W.; Nakajima, H., et al., Synthesis of a Bimetallic Dodecaborate $LiNaB_{12}H_{12}$ with Outstanding Superionic Conductivity. *Chem. Mater.,* **2015,** *27* (16), 5483-5486.

(58) Jørgensen, M.; Jensen, S. R. H.; Humphries, T. D., et al., Hydroxylated closo-Dodecaborates $M_2B_{12}(OH)_{12}$ (M = Li, Na, K, and Cs); Structural Analysis, Thermal Properties, and Solid-State Ionic Conductivity. *J. Phys. Chem. C,* **2020,** *124* (21), 11340-11349.

(59) Jung, D.; Muni, M.; Marin, G., et al., Enhancing cycling stability of tungsten oxide supercapacitor electrodes via a boron cluster-based molecular cross-linking approach. *J. Mater. Chem. A,* **2020,** *8* (35), 18015-18023.

(60) Jung, D.; Saleh, L. M. A.; Berkson, Z. J., et al., A molecular cross-linking approach for hybrid metal oxides. *Nat. Mater.,* **2018,** *17* (4), 341-348.

(61) Ready, A. D.; Becwar, S. M.; Jung, D., et al., Synthesis and structural properties of a 2D Zn(II) dodecahydroxy-closo-dodecaborate coordination polymer. *Dalton Trans.,* **2022,** *51* (30), 11547-11557.

(62) Jørgensen, M.; Hansen, B. R. S.; Lee, Y.-S., et al., Crystal Structures and Energy Storage Properties of Ammine Sodium Decahydro-closo-decaboranes ($Na_2B_{10}H_{10}{\cdot}nNH_3$, n = 1, 2). *J. Phys. Chem. C,* **2019,** *123* (33), 20160-20166.

(63) Paskevicius, M.; Hansen, B. R. S.; Jørgensen, M., et al., Multifunctionality of silver closo-boranes. *Nat. Commun.,* **2017,** *8* (1), 15136.

(64) Tang, W. S.; Matsuo, M.; Wu, H., et al., Stabilizing lithium and sodium fast-ion conduction in solid polyhedral-borate salts at device-relevant temperatures. *Energy Storage Mater.,* **2016,** *4*, 79-83.

(65) Yoshida, K.; Sato, T.; Unemoto, A., et al., Fast sodium ionic conduction in $Na_2B_{10}H_{10}$-$Na_2B_{12}H_{12}$ pseudo-binary complex hydride and application to a bulk-type all-solid-state battery. *Appl. Phys. Lett.,* **2017,** *110* (10), 103901.

(66) Toyama, N.; Kim, S.; Oguchi, H., et al., Lithium ion conductivity of complex hydrides incorporating multiple closo-type complex anions. *J. Energy Chem.,* **2019,** *38*, 84-87.

(67) Kim, S.; Kisu, K.; Takagi, S., et al., Complex Hydride Solid Electrolytes of the $Li(CB_9H_{10})$–$Li(CB_{11}H_{12})$ Quasi-Binary System: Relationship between the Solid Solution and Phase Transition, and the Electrochemical Properties. *ACS Appl. Energy Mater.,* **2020,** *3* (5), 4831-4839.

(68) Hansen, B. R. S.; Paskevicius, M.; Jørgensen, M.; Jensen, T. R., Halogenated Sodium-closo-Dodecaboranes as Solid-State Ion Conductors. *Chem. Mater.,* **2017,** *29* (8), 3423-3430.

(69) Sadikin, Y.; Schouwink, P.; Brighi, M., et al., Modified Anion Packing of $Na_2B_{12}H_{12}$ in Close to Room Temperature Superionic Conductors. *Inorg. Chem.,* **2017,** *56* (9), 5006-5016.

(70) Duchêne, L.; Kühnel, R. S.; Rentsch, D., et al., A highly stable sodium solid-state electrolyte based on a dodeca/deca-borate equimolar mixture. *Chem. Commun.,* **2017,** *53* (30), 4195-4198.

(71) Tang, W. S.; Yoshida, K.; Soloninin, A. V., et al., Stabilizing Superionic-Conducting Structures via Mixed-Anion Solid Solutions of Monocarba-closo-borate Salts. *ACS Energy Lett.,* **2016,** *1* (4), 659-664.

(72) Payandeh, S.; Asakura, R.; Avramidou, P., et al., Nido-Borate/Closo-Borate Mixed-Anion Electrolytes for All-Solid-State Batteries. *Chem. Mater.,* **2020,** *32* (3), 1101-1110.

(73) Kim, S.; Oguchi, H.; Toyama, N., et al., A complex hydride lithium superionic conductor for high-energy-density all-solid-state lithium metal batteries. *Nat. Commun.,* **2019,** *10* (1), 1081.

(74) Brighi, M.; Murgia, F.; Łodziana, Z., et al., A mixed anion hydroborate/carba-hydroborate as a room temperature Na-ion solid electrolyte. *J. Power Sources,* **2018,** *404*, 7-12.

(75) Asakura, R.; Duchêne, L.; Kühnel, R.-S., et al., Electrochemical Oxidative Stability of Hydroborate-Based Solid-State Electrolytes. *ACS Appl. Energy Mater.,* **2019,** *2* (9), 6924-6930.

(76) Duchêne, L.; Kühnel, R. S.; Stilp, E., et al., A stable 3 V all-solid-state sodium–ion battery based on a closo-borate electrolyte. *Energy & Environmental Science,* **2017,** *10* (12), 2609-2615.

(77) Duchêne, L.; Remhof, A.; Hagemann, H.; Battaglia, C., Status and prospects of hydroborate electrolytes for all-solid-state batteries. *Energy Storage Mater.,* **2020,** *25*, 782-794.

(78) Unemoto, A.; Ikeshoji, T.; Yasaku, S., et al., Stable Interface Formation between TiS_2 and $LiBH_4$ in Bulk-Type All-Solid-State Lithium Batteries. *Chem. Mater.,* **2015,** *27* (15), 5407-5416.

(79) Li, S.; Qiu, P.; Kang, J., et al., Iodine-Substituted Lithium/Sodium closo-Decaborates: Syntheses, Characterization, and Solid-State Ionic Conductivity. *ACS Appl. Mater. Interfaces,* **2021,** *13* (15), 17554-17564.

(80) Černý, R.; Murgia, F.; Brighi, M., Metal hydroborates: From hydrogen stores to solid electrolytes. *J. Alloys Compd.,* **2022,** *895*, 162659.

(81) Tang, W. S.; Matsuo, M.; Wu, H., et al., Liquid-Like Ionic Conduction in Solid Lithium and Sodium Monocarba-closo-Decaborates Near or at Room Temperature. *Adv. Energy Mater.,* **2016,** *6* (8), 1502237.

(82) Cuan, J.; Zhou, Y.; Zhou, T., et al., Borohydride-Scaffolded Li/Na/Mg Fast Ionic Conductors for Promising Solid-State Electrolytes. *Adv. Mater.,* **2019,** *31* (1), 1803533.

(83) H. P. Souza, D.; Møller, K. T.; Moggach, S. A., et al., Hydrated alkali-$B_{11}H_{14}$ salts as potential solid-state electrolytes. *J. Mater. Chem. A,* **2021,** *9* (26), 15027-15037.

(84) Lu, Z.; Ciucci, F., Metal Borohydrides as Electrolytes for Solid-State Li, Na, Mg, and Ca Batteries: A First-Principles Study. *Chem. Mater.,* **2017,** *29* (21), 9308-9319.

(85) Dimitrievska, M.; Wu, H.; Stavila, V., et al., Structural and Dynamical Properties of Potassium Dodecahydro-monocarba-closo-dodecaborate: $KCB_{11}H_{12}$. *J. Phys. Chem. C,* **2020,** *124* (33), 17992-18002.

(86) Sadikin, Y.; Skoryunov, R. V.; Babanova, O. A., et al., Anion Disorder in $K_3BH_4B_{12}H_{12}$ and Its Effect on Cation Mobility. *J. Phys. Chem. C,* **2017,** *121* (10), 5503-5514.

(87) Niitani, K.; Ushiroda, S.; Kuwata, H., et al., Hard Carbon Anode with a Sodium Carborane Electrolyte for Fast-Charging All-Solid-State Sodium-Ion Batteries. *ACS Energy Lett.,* **2022,** *7* (1), 145-149.

(88) Keener, M.; Mattejat, M.; Zheng, S.-L., et al., Selective electrochemical capture and release of uranyl from aqueous alkali, lanthanide, and actinide mixtures using redox-switchable carboranes. *Chem. Sci.,* **2022,** *13* (12), 3369-3374.

(89) Keener, M.; Hunt, C.; Carroll, T. G., et al., Redox-switchable carboranes for uranium capture and release. *Nature,* **2020,** *577* (7792), 652-655.

(90) Michl, J., Chemistry of the three-dimensionally aromatic CB_{11} cage. *Pure Appl. Chem.,* **2008,** *80* (3), 429-446.

(91) Fete, M. G.; Havlas, Z.; Michl, J., $HCB_{11}(CF_3)_nF_{11-n}^-$: Inert Anions with High Anodic Oxidation Potentials. *J. Am. Chem. Soc.,* **2011,** *133* (11), 4123-4131.

(92) Boeré, R. T.; Derendorf, J.; Jenne, C., et al., On the Oxidation of the Three-Dimensional Aromatics $[B_{12}X_{12}]^{2-}$ (X=F, Cl, Br, I). *Chem. Eur. J.,* **2014,** *20* (15), 4447-4459.

(93) Bukovsky, E. V.; Peryshkov, D. V.; Wu, H., et al., Comparison of the Coordination of $B_{12}F_{12}^{2-}$, $B_{12}Cl_{12}^{2-}$, and $B_{12}H_{12}^{2-}$ to Na^+ in the Solid State: Crystal Structures and Thermal Behavior of $Na_2(B_{12}F_{12})$, $Na_2(H_2O)_4(B_{12}F_{12})$, $Na_2(B_{12}Cl_{12})$, and $Na_2(H_2O)_6(B_{12}Cl_{12})$. *Inorg. Chem.,* **2017,** *56* (8), 4369-4379.

(94) Lacroix, M. R.; Bukovsky, E. V.; Lozinšek, M., et al., Manifestations of Weak O–H···F Hydrogen Bonding in $M(H_2O)_n(B_{12}F_{12})$ Salt Hydrates: Unusually Sharp Fourier Transform Infrared ν(OH) Bands and Latent Porosity (M = Mg–Ba, Co, Ni, Zn). *Inorg. Chem.,* **2018,** *57* (23), 14983-15000.

(95) Qian, E. A.; Wixtrom, A. I.; Axtell, J. C., et al., Atomically precise organomimetic cluster nanomolecules assembled via perfluoroaryl-thiol SNAr chemistry. *Nat. Chem.,* **2017,** *9* (4), 333-340.

(96) Wixtrom, A. I.; Shao, Y.; Jung, D., et al., Rapid synthesis of redox-active dodecaborane $B_{12}(OR)_{12}$ clusters under ambient conditions. *Inorg. Chem. Front.,* **2016,** *3* (5), 711-717.

(97) Wixtrom, A. I.; Parvez, Z. A.; Savage, M. D., et al., Tuning the electrochemical potential of perfunctionalized dodecaborate clusters through vertex differentiation. *Chem. Commun.,* **2018,** *54* (46), 5867-5870.

(98) Shida, N.; Owaki, S.; Eguchi, H., et al., Bis(pentafluorophenyl)-o-carborane and its arylthio derivatives: synthesis, electrochemistry and optical properties. *Dalton Trans.,* **2020,** *49* (37), 12985-12989.

(99) Farha, O. K.; Julius, R. L.; Lee, M. W., et al., Synthesis of Stable Dodecaalkoxy Derivatives of hypercloso-$B_{12}H_{12}$. *J. Am. Chem. Soc.,* **2005,** *127* (51), 18243-18251.

(100) Hawthorne, M. F.; Pushechnikov, A., Polyhedral borane derivatives: Unique and versatile structural motifs. *Pure Appl. Chem.,* **2012,** *84* (11), 2279-2288.

(101) Lee, M. W.; Farha, O. K.; Hawthorne, M. F.; Hansch, C. H., Alkoxy Derivatives of Dodecaborate: Discrete Nanomolecular Ions with Tunable Pseudometallic Properties. *Angew. Chem. Int. Ed.,* **2007,** *46* (17), 3018-3022.

(102) Li, B.; Zhang, X.; Stauber, J. M., et al., Electronic Structure of Superoxidized Radical Cationic Dodecaborate-Based Clusters. *J. Phys. Chem. A,* **2021,** *125* (28), 6141-6150.

(103) Messina, M. S.; Axtell, J. C.; Wang, Y., et al., Visible-Light-Induced Olefin Activation Using 3D Aromatic Boron-Rich Cluster Photooxidants. *J. Am. Chem. Soc.,* **2016,** *138* (22), 6952-6955.

(104) Peymann, T.; Knobler, C. B.; Khan, S. I.; Hawthorne, M. F., Dodeca(benzyloxy)dodecaborane, $B_{12}(OCH_2Ph)_{12}$: A Stable Derivative of hypercloso-$B_{12}H_{12}$. *Angew. Chem. Int. Ed.,* **2001,** *40* (9), 1664-1667.

(105) Spokoyny, A. M., New ligand platforms featuring boron-rich clusters as organomimetic substituents. *Pure Appl. Chem.,* **2013,** *85* (5), 903.

(106) Stauber, J. M.; Qian, E. A.; Han, Y., et al., An Organometallic Strategy for Assembling Atomically Precise Hybrid Nanomaterials. *J. Am. Chem. Soc.,* **2020,** *142* (1), 327-334.

(107) Stauber, J. M.; Schwan, J.; Zhang, X., et al., A Super-Oxidized Radical Cationic Icosahedral Boron Cluster. *J. Am. Chem. Soc.,* **2020,** *142* (30), 12948-12953.

(108) Barton, J. L.; Wixtrom, A. I.; Kowalski, J. A., et al., Perfunctionalized Dodecaborate Clusters as Stable Metal-Free Active Materials for Charge Storage. *ACS Appl. Energy Mater.,* **2019,** *2* (7), 4907-4913.

(109) Kim, Y.; Kubena, R.; Axtell, J., et al., Dynamic Nuclear Polarization Using 3D Aromatic Boron Cluster Radicals. *J. Phys. Chem. Lett.,* **2021,** *12* (1), 13-18.

(110) Qian, E. A.; Han, Y.; Messina, M. S., et al., Multivalent Cluster Nanomolecules for Inhibiting Protein–Protein Interactions. *Bioconjugate Chem.,* **2019,** *30* (10), 2594-2603.

(111) Axtell, J. C.; Messina, M. S.; Liu, J.-Y., et al., Photooxidative Generation of Dodecaborate-Based Weakly Coordinating Anions. *Inorg. Chem.,* **2019,** *58* (16), 10516-10526.

(112) Goswami, L. N.; Everett, T. A.; Khan, A. A.; Hawthorne, M. F., Rational Design of a Stable Two One-Electron Redox-Active closo-Dodecaalkoxyborane Ion as Biothiol Sensor. *Eur. J. Inorg. Chem.,* **2020,** *2020* (4), 377-381.

(113) Aubry, T. J.; Axtell, J. C.; Basile, V. M., et al., Dodecaborane-Based Dopants Designed to Shield Anion Electrostatics Lead to Increased Carrier Mobility in a Doped Conjugated Polymer. *Adv. Mater.,* **2019,** *31* (11), 1805647.

(114) Aubry, T. J.; Winchell, K. J.; Salamat, C. Z., et al., Tunable Dopants with Intrinsic Counterion Separation Reveal the Effects of Electron Affinity on Dopant Intercalation and Free Carrier Production in Sequentially Doped Conjugated Polymer Films. *Adv. Funct. Mater.,* **2020,** *30* (28), 2001800.

(115) Muetterties, E. L.; Balthis, J. H.; Chia, Y. T., et al., Chemistry of Boranes. VIII. Salts and Acids of $B_{10}H_{10}^{2-}$ and $B_{12}H_{12}^{2-}$. *Inorg. Chem.,* **1964,** *3* (3), 444-451.

(116) McKee, M. L., Density Functional Theory Study of Anionic and Neutral Per-Substituted 12-Vertex Boron Cage Systems, $B_{12}X_{12}^{n-}$ (n = 2, 1, 0). *Inorg. Chem.,* **2002,** *41* (5), 1299-1305.

(117) Tan, J.; Ao, X.; Dai, A., et al., Polycation ionic liquid tailored PEO-based solid polymer electrolytes for high temperature lithium metal batteries. *Energy Storage Mater.,* **2020,** *33*, 173-180.

(118) Zhou, W.; Wang, Z.; Pu, Y., et al., Double-Layer Polymer Electrolyte for High-Voltage All-Solid-State Rechargeable Batteries. *Adv. Mater.,* **2019,** *31* (4), 1805574.

(119) Elizalde-Segovia, R.; Irshad, A.; Zayat, B.; Narayanan, S. R., Solid-State Lithium-Sulfur Battery Based on Composite Electrode and Bi-layer Solid Electrolyte Operable at Room Temperature. *J. Electrochem. Soc.,* **2020,** *167* (14), 140529.

(120) Irshad, A.; Elizalde-Segovia, R.; Jayathilake, B. S., et al., Understanding the Role of Carbon Mixtures on the Polarization of Sulfur Electrodes in Lithium-Sulfur Batteries. *J. Electrochem. Soc.,* **2022,** *169* (11), 110528.

(121) Hansen, C. J.; Zak, J. J.; Martinolich, A. J., et al., Multielectron, Cation and Anion Redox in Lithium-Rich Iron Sulfide Cathodes. *J. Am. Chem. Soc.,* **2020,** *142* (14), 6737-6749.

Table of Contents Figure (TOC):

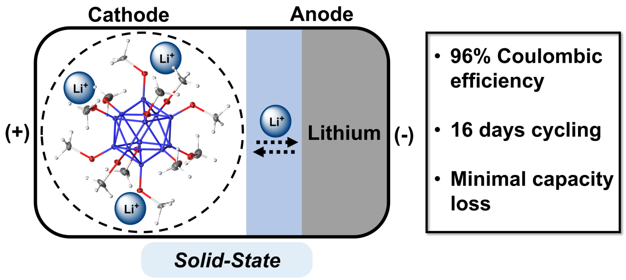

Supporting Information

Electrochemical Cycling of Redox-Active Boron Cluster-Based Materials in the Solid State

Austin D. Ready,[a†] Ahamed Irshad,[b†] Anna Kallistova,[c] Moises Carrillo,[a] Milan Gembicky,[e] Ram Seshadri,[c,d] Sri Narayan,[b] Alexander M. Spokoyny*[a,f]*

[a]Department of Chemistry and Biochemistry, University of California, Los Angeles, Los Angeles, CA 90095, USA

[b]Department of Chemistry and Loker Hydrocarbon Research Institute, University of Southern California, Los Angeles, CA 90089, USA

[c]Materials Department and Materials Research Laboratory, University of California, Santa Barbara, Santa Barbara, CA 93106, USA

[d]Department of Chemistry and Biochemistry, University of California, Santa Barbara, Santa Barbara, CA 93106, USA

[e]Department of Chemistry and Biochemistry, University of California, San Diego, La Jolla, CA 92521, USA

[f]California NanoSystems Institute (CNSI), University of California, Los Angeles, CA 90095, USA

[†]These authors contributed equally

*To whom correspondence should be addressed: spokoyny@chem.ucla.edu; srnaraya@usc.edu

Table of Contents

I. General Information

Methods and Materials

Reagent Information:

All commercially available chemicals were used as received unless otherwise noted. Dry THF, Et_2O, and CH_3CN were obtained from a Grubbs column with activated alumina and copper catalyst, and then stored over 4Å molecular sieves in a nitrogen-filled glovebox. The synthesis and purification of $Li_2[B_{12}(OCH_3)_{12}]$ was performed in a nitrogen-filled glovebox. All other manipulations were performed in air using unpurified solvents unless otherwise stated. Trimethylsulfoxonium bromide (>98.0%) was purchased from TCI America and used as received. Dichloromethane (≥99.5%), hexanes (≥98.5%), Ammonium cerium (IV) nitrate (≥98.5%), and N,N-diisopropylethylamine (≥99%, SureSeal) were purchased from Sigma-Aldrich and used as received. Methyllithium solution (1.6 M in Et_2O) was purchased from Sigma-Aldrich, stored in a -30°C freezer in a nitrogen-filled glovebox, and used as received. Tetrabutylammonium hexafluorophosphate (98%) was purchased from Sigma-Aldrich, recrystallized three times from hot ethanol, dried at 80°C under vacuum, and stored in a desiccator prior to use as an electrolyte for electrochemical measurements.

Analytical Instrumentation:

NMR

NMR spectra were measured on a Bruker AV400 spectrometer at 400 MHz (^1H) 125 MHz (^{13}C), and 128 MHz (^{11}B), reported in δ (parts per million) relative to tetramethylsilane (^1H, ^{13}C) or $BF_3{\cdot}Et_2O$ (^{11}B), and referenced to residual ^1H /^{13}C signals solvent signals (^1H (δ) $CDCl_3$ 7.26, D_2O 4.79; ^{13}C (δ) $CDCl_3$ 77.16; ^{11}B (δ) $BF_3{\cdot}Et_2O$ 0.00 ppm. Deuterated solvents were purchased from Cambridge Isotope Laboratories and used as received. Spectra were processed using MestReNova Version 6.0.2.

PXRD

Powder x-ray diffraction measurements were measured using a Panalytical X'Pert Pro X-ray Powder Diffractometer (Cu-Kα 1.5406 Å). Samples were deposited as dry powders onto a zero-background sample holder, and then diffracted from 5° to 70° 2θ with a step size of 0.016° and a 2° nickel filter.

Synchrotron Powder Diffraction

High resolution synchrotron powder diffraction data were collected using beamline 11-BM at the Advanced Photon Source (APS), Argonne National Laboratory using an average wavelength of 0.41 Å. Discrete detectors covering an angular range from -6 to 16 ° 2θ were scanned over a 34° 2θ range, with data points collected every 0.001° 2θ and scan speed of 0.01°/s.

TGA

Thermogravimetric analysis was performed on a Perkin-Elmer TGA8000. Approximately 5 mg of sample was analyzed in an alumina crucible for each measurement. Samples were heated from 30° to 350° C at a rate of 10°C/min under a constant N_2 flow of 40 mL/min.

FTIR

Fourier-Transform IR measurements were measured on an Agilent Cary 630 FTIR Spectrometer. After a background scan, samples were analyzed as a powder using 64 scans.

XPS

X-ray photoelectron spectroscopy (XPS) measurements were performed on an AXIS Ultra DLD instrument (Kratos Analytical Inc.). Spectra were obtained using a monochromatic AI Kα X-ray source (Filament current: 1.8 A) with a 10 mA emission current and an anode voltage of 15 kV. Survey spectra were conducted with a pass energy of 160 eV, 1 eV step size, and 100 ms dwell time. High-resolution spectra were generally conducted with a pass energy of 20 eV, 1 eV step size, and 600 ms dwell time. All spectra were measured with automatic charge neutralization and referenced to the adventitious carbon 1s signal at 284.6 eV. XPS data was further processed using CasaXPS.

Microwave Reactor

Microwave reactions were performed on a CEM Discover 2.0 Microwave synthesis reactor. All reactions were performed in a 30 mL microwave vial with a silicone/PTFE cap purchased from CEM and a rare-earth PTFE-coated stir bar. Reaction mixtures were premixed for 30 seconds and then heated to 120°C with a 3 minute temperature ramp and held at temperature for 1 hour. The maximum pressure release limit was 250 psi and the maximum wattage was 250 W. The power was applied dynamically by the microwave and did not exceed this limit.

Mass Spectrometry

Mass spectra were collected using Electrospray Ionization on a Waters LCT Premier Mass Spectrometer. Samples were prepared by taking a few drops of analyte dissolved in $CDCl_3$ and diluting to an appropriate concentration with CH_3CN, with a typical injection volume of 2.0 μL.

Cyclic Voltammetry

Cyclic voltammetry was performed with a Gamry Frameworks Interface 1010E Potentiostat. Measurements were performed using a CH instruments glassy carbon working electrode, Pt wire counter electrode, and an Ag/Ag^+ pseudo-reference electrode. Prior to measurements, the glassy carbon working electrode was polished using an alumina polishing solution, and the Pt and Ag wires were polished using Buehler 500 grit silicon carbide sandpaper. In the glass body, the

Ag/Ag$^+$ pseudo-reference contained a freshly polished Ag wire in a saturated KCl solution of dry CH_3CN. This was separated from the analyte solution by a BASi CoralPor® tip. All experiments were conducted in a 0.1 M [TBA]PF_6 (recrystallized 3 times) electrolyte solution in 5 mL of dry DCM (dried on a Grubbs column with activated alumina and copper catalyst). The electrolyte solution was thoroughly sparged with nitrogen gas for 30 minutes prior to running measurements. Cyclic voltammograms of $B_{12}(OCH_3)_{12}$ were performed at a 3mM concentration, with a scan rate of 25 mV/s, step size of 1 mV, and an equilibration time of 5 seconds. After collecting analyte data, ~1 mg ferrocene (Alfa Aesar, 99%) was added to the analyte solution as an internal reference, and additional voltammograms were measured. The analyte half-wave potentials were then referenced to the Fc/Fc$^+$ redox couple. The cyclic voltammogram currents presented in the main text were smoothed using a Savitzky-Golay filter (4th order, 16-point width), followed by a sliding window filter (20-point width). Raw, unedited voltammograms are provided below.

II. Synthesis of $B_{12}(OCH_3)_{12}$ and $Li_2[B_{12}(OCH_3)_{12}]$

Synthesis of $B_{12}(OCH_3)_{12}$

$TBA_2B_{12}(OH)_{12}$ was synthesized via cation exchange from $Cs_2B_{12}(OH)_{12}$, as previously reported[1]. $B_{12}(OCH_3)_{12}$ was synthesized by expanding on our previously established microwave reaction method[2-3].

Note: $B_{12}(OCH_3)_{12}$ was studied computationally via DFT by McKee[4] in 2002, and its synthesis/isolation was first reported by Farha et al.[1] in 2005. However, it was only obtained in 50% yield and was not characterized crystallographically. Additionally, the previous method used methyl tosylate and aggressive reaction conditions (Argon atmosphere, 2 h at 150°C and

1300 psi in a glass-lined autoclave vessel) followed by Fe(III) oxidation and column chromatography.

$TBA_2B_{12}(OH)_{12}$ (60 mg, 0.072 mmol) was weighed out in a nitrogen-filled glovebox, dissolved in 6 mL dry CH_3CN, brought out into air and transferred to an oven-dried 30 mL CEM microwave reaction vial, along with a rare-earth stir bar. N, N-Diisopropylethylamine (1.2 mL, 6.89 mmol, 95.7 equiv.) was added via syringe, followed by trimethylsulfoxonium bromide (1.246 g, 7.2 mmol, 100 equiv.). The microwave vial was placed in a CEM Discover 2.0 microwave reactor, heated to 120°C over a period of 3 minutes, and then held at that temperature for 1 hour. The resulting solution is a deep red color, indicative of the radical anion species. The microwave reaction was performed three more times on the same 60 mg scale, and all four reaction mixtures were combined. The solvent was removed under reduced pressure with heating to 50°C, then washed with 3 x 20 mL hexanes to remove excess base. The remaining viscous red compound was dried under high vacuum for 8 hours to give $B_{12}(OCH_3)_{12}$ as a mixture of 2- and 1- oxidation states. Note that the 1- radical anion is spectroscopically silent. ^{11}B NMR: (128 MHz, $CDCl_3$): δ -16.8 ppm.

Oxidation of $[B_{12}(OCH_3)_{12}]^{2-/1-}$ to $[B_{12}(OCH_3)_{12}]^0$

The red solid was dissolved in 25 mL MilliQ H_2O with stirring. Cerium (IV) ammonium nitrate (0.625 g, 1.14 mmol) was dissolved separately in 13 mL MilliQ H_2O, and this solution was added dropwise to the reaction mixture. The immediate precipitation of neutral $B_{12}(OCH_3)_{12}$ was observed, along with a color change in the solution from dark red to orange. The reaction mixture was stirred vigorously for 5 hours. The precipitate was then collected on a fritted funnel via vacuum filtration and washed with copious amounts of cold MilliQ water, followed by 3 x 5 mL cold CH_3CN to remove any unoxidized cluster. The compound was left to dry on the frit for

1 hour and then collected with DCM and dried with anhydrous $MgSO_4$. The solution was then filtered, and the solvent removed under reduced pressure. The boron cluster was further dried in a flask under reduced pressure on a Schlenk line in a 90°C oil bath for 3 hours to give 101 mg of $B_{12}(OCH_3)_{12}$ (0.20 mmol, 70% yield). $B_{12}(OCH_3)_{12}$ is a dark orange-red powder which sublimes at 100°C under vacuum and can be recrystallized from a saturated DCM solution to give rhomboid-shaped dark orange-red crystallites. ^{11}B NMR (128 MHz, $CDCl_3$): δ 38.0 ppm; ^{1}H NMR (400 MHz, $CDCl_3$): δ 3.84 ppm (s, 36 H); ^{13}C NMR (125 MHz, $CDCl_3$): δ 59.0 ppm. ESI-MS (CH_3CN): m/z calculated for $C_{12}H_{36}B_{12}O_{12}$ [M^-] = 502.34, observed = 502.34.

Synthesis of $Li_2[B_{12}(OCH_3)_{12}]$

50 mg of dry $B_{12}(OCH_3)_{12}$ was brought into a nitrogen-filled glovebox, transferred into an oven-dried Schlenk flask equipped with a stir bar, and dissolved in approximately 100 mL dry THF with vigorous stirring. Once completely dissolved, 0.50 mL of CH_3Li solution (1.2 M in Et_2O) was added via syringe. The reaction mixture immediately changed color from dark orange to red and then colorless, with formation of a white precipitate. The mixture was left to stir for 1 hour and then the solvent was removed under reduced pressure. The remaining solid was washed with 3 x 10 mL dry Et_2O to remove any unreacted CH_3Li, and dried under reduced pressure to give $Li_2[B_{12}(OCH_3)_{12}]_{12}$ as a white powder (40 mg, 0.078 mmol, 78% yield). ^{11}B NMR (128 MHz, D_2O): δ -16.0 ppm; ^{1}H NMR (400 MHz., D_2O): δ 3.62 ppm singlet. ESI-MS (D_2O): m/z calculated for $C_{12}H_{36}B_{12}O_{12}$ [M^-] = 502.34, observed = 502.33.

III. Characterization of $B_{12}(OCH_3)_{12}$

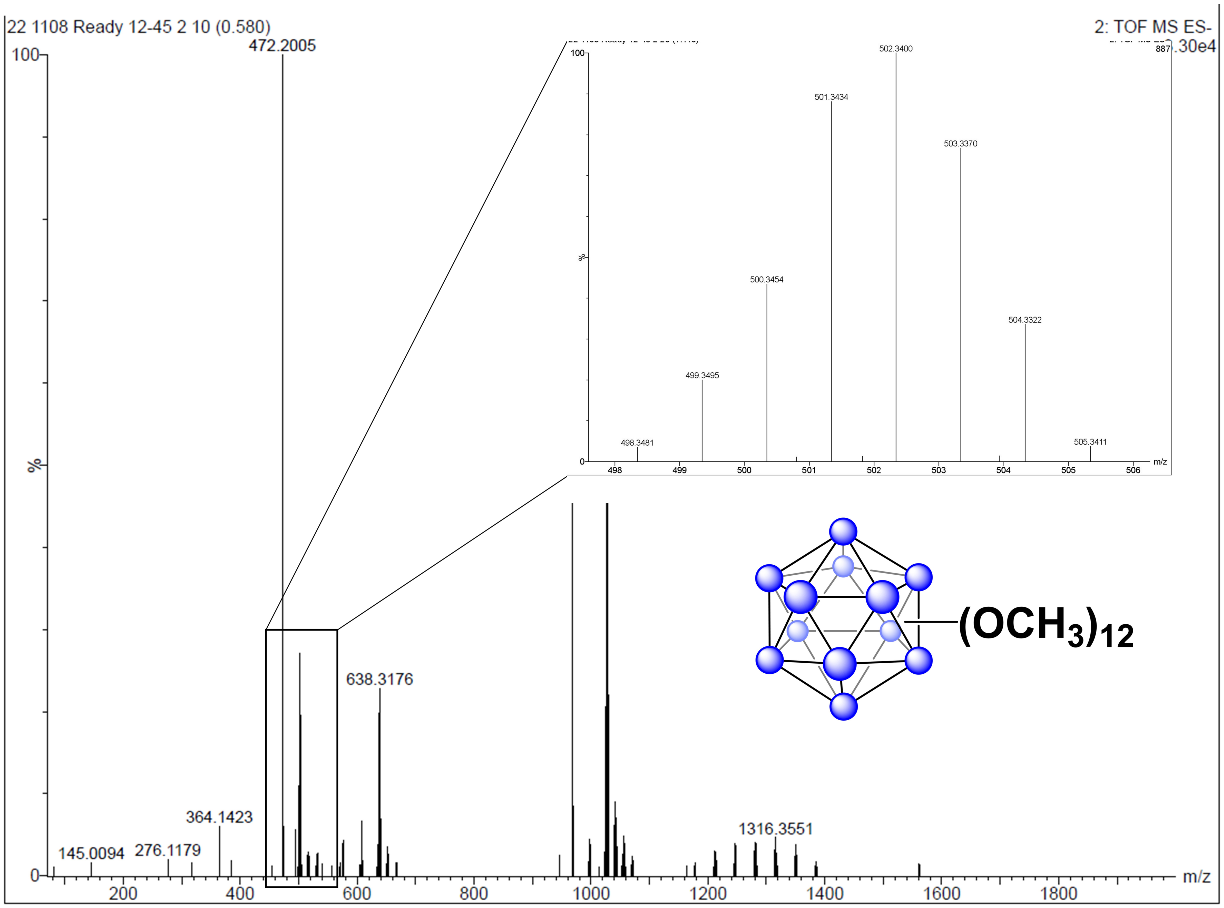

Figure S1. Full mass spectrum of $B_{12}(OCH_3)_{12}$ in CH_3CN; electrospray ionization, negative mode; observed as $[M]^-$.

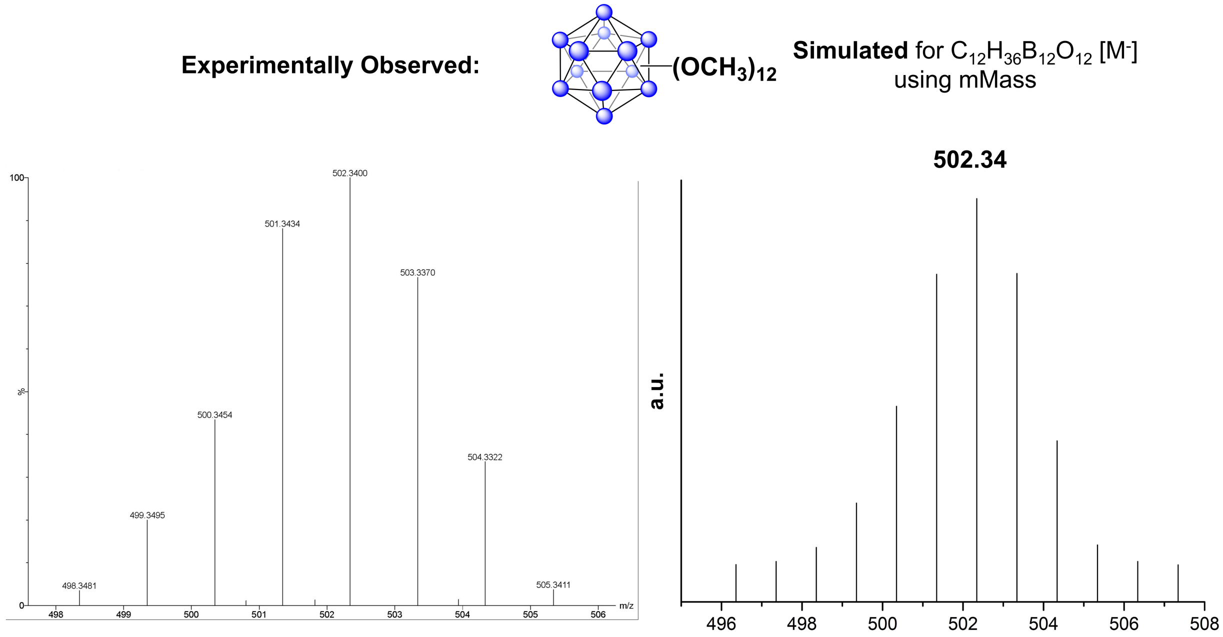

Figure S2. Zoomed in mass spectrum of $B_{12}(OCH_3)_{12}$ in CH_3CN as compared to simulated spectrum; observed as $[M]^-$.

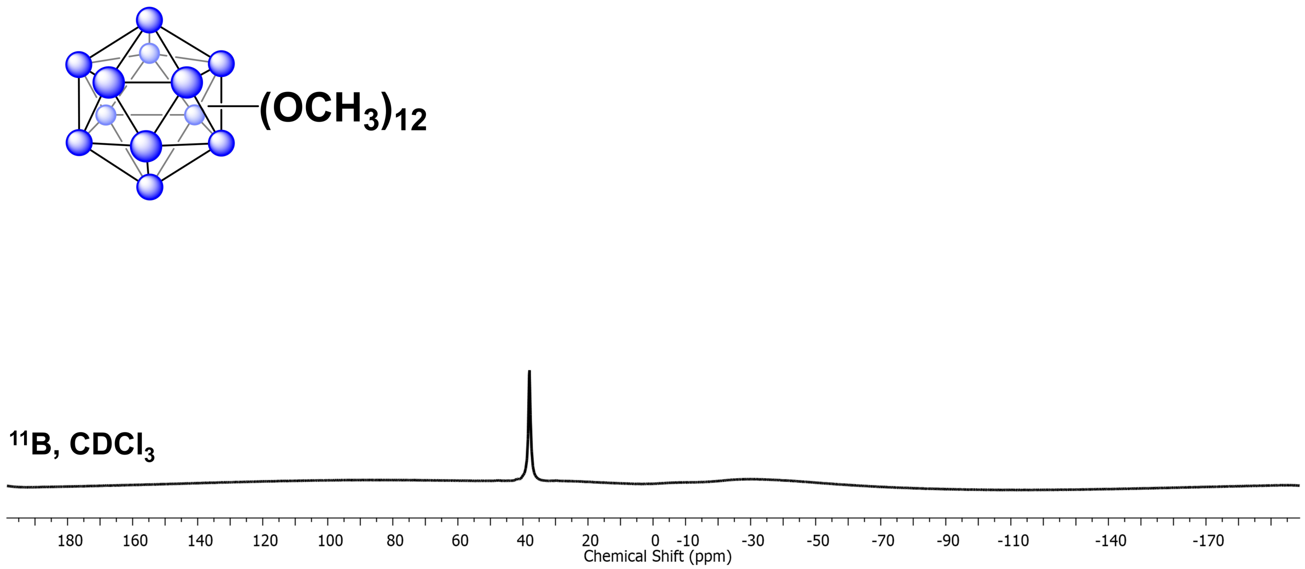

Figure S3. ^{11}B NMR spectrum of $[B_{12}(OCH_3)_{12}]^0$ in $CDCl_3$.

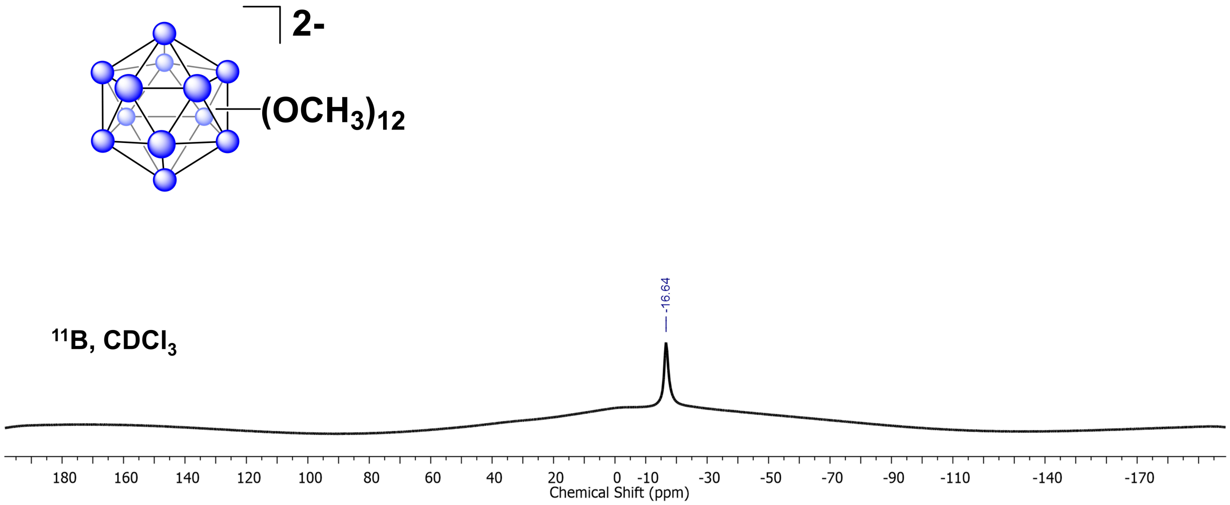

Figure S4. ^{11}B NMR spectrum of crude reaction mixture from microwave synthesis of $[B_{12}(OCH_3)_{12}]^{1-/2-}$. Note that the 1- radical anion is spectroscopically silent.

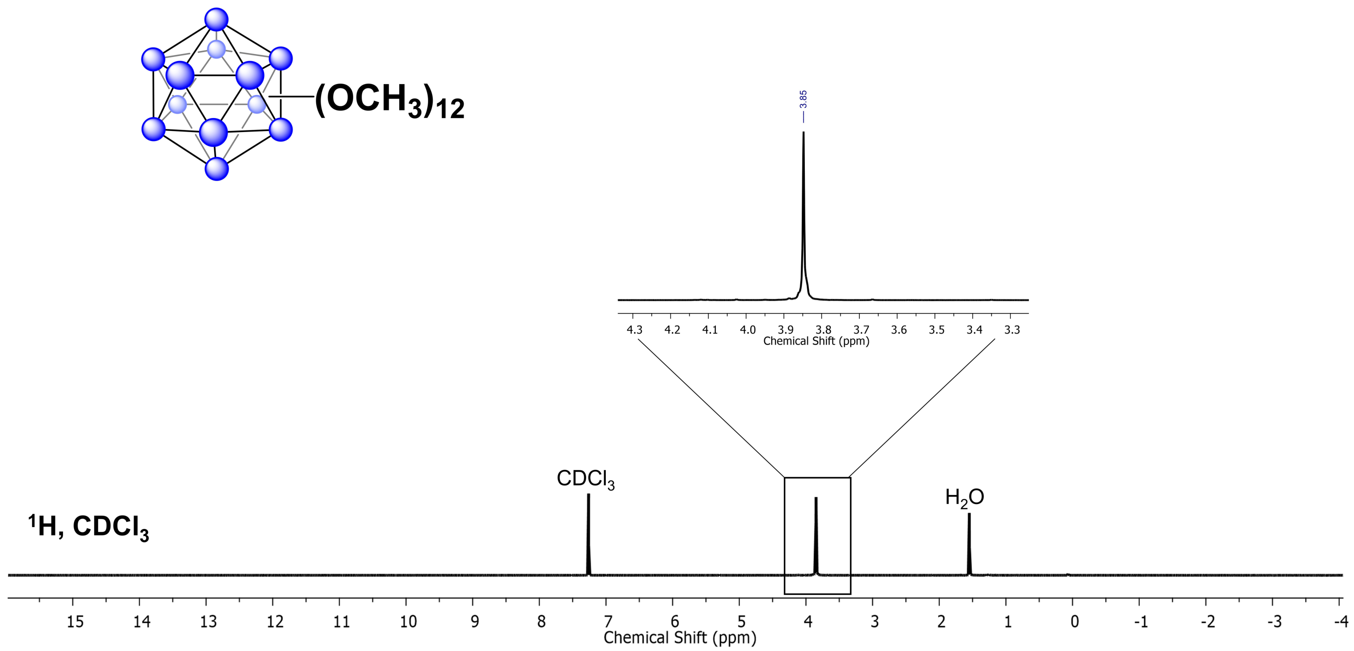

Figure S5. ^{1}H NMR spectrum of $[B_{12}(OCH_3)_{12}]^0$ in $CDCl_3$.

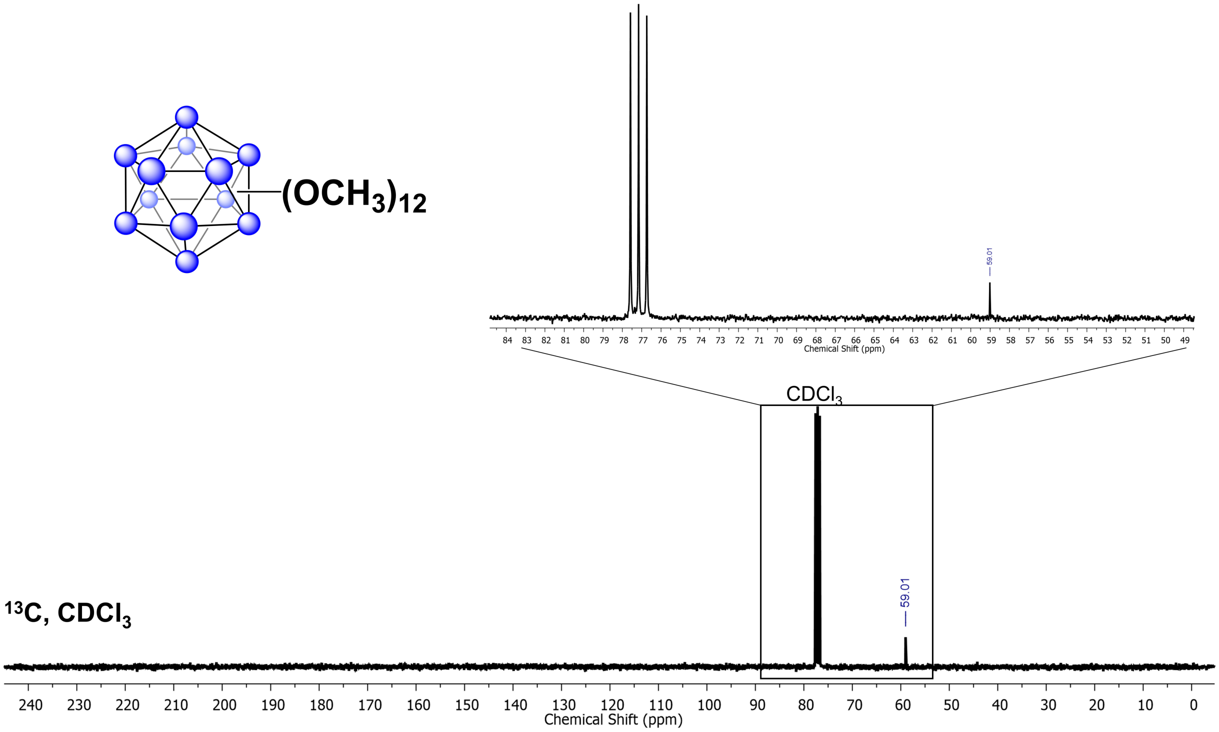

Figure S6. ^{13}C NMR spectrum of $[B_{12}(OCH_3)_{12}]^0$ in $CDCl_3$.

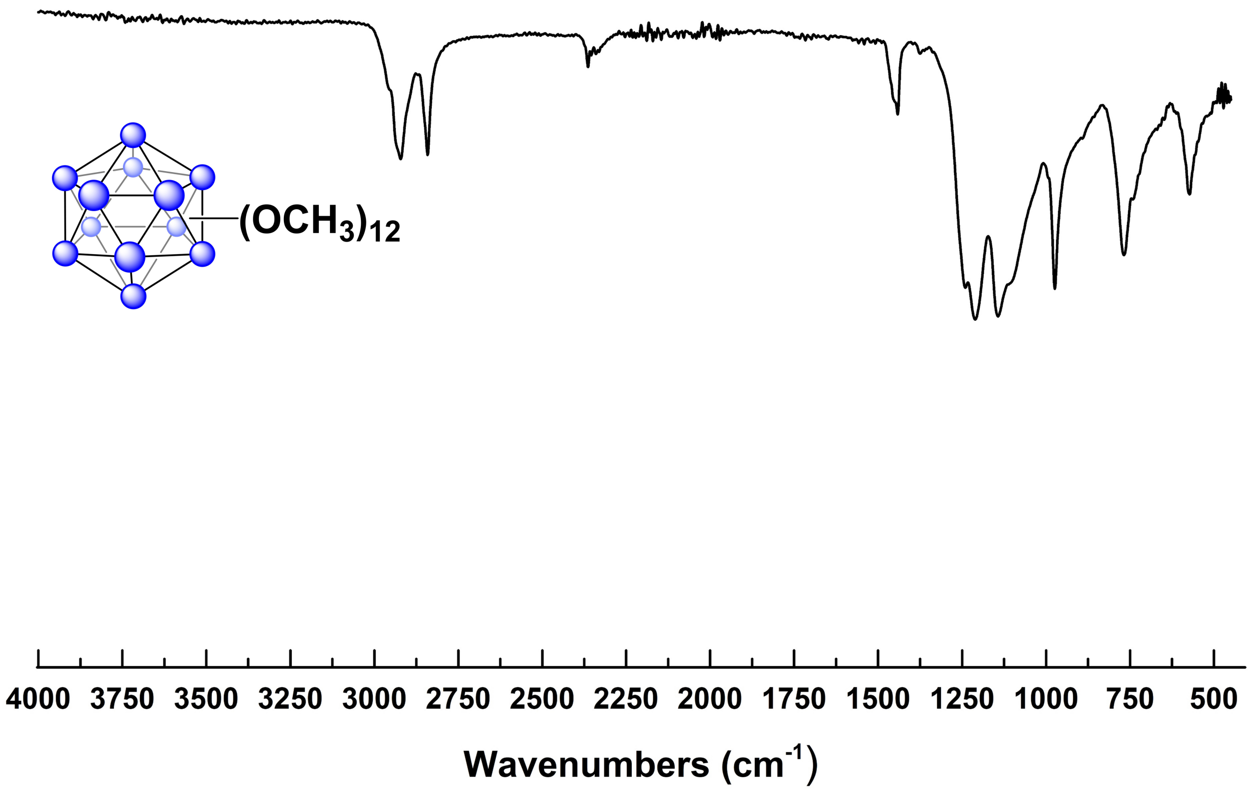

Figure S7. FTIR of a powder sample of $B_{12}(OCH_3)_{12}$.

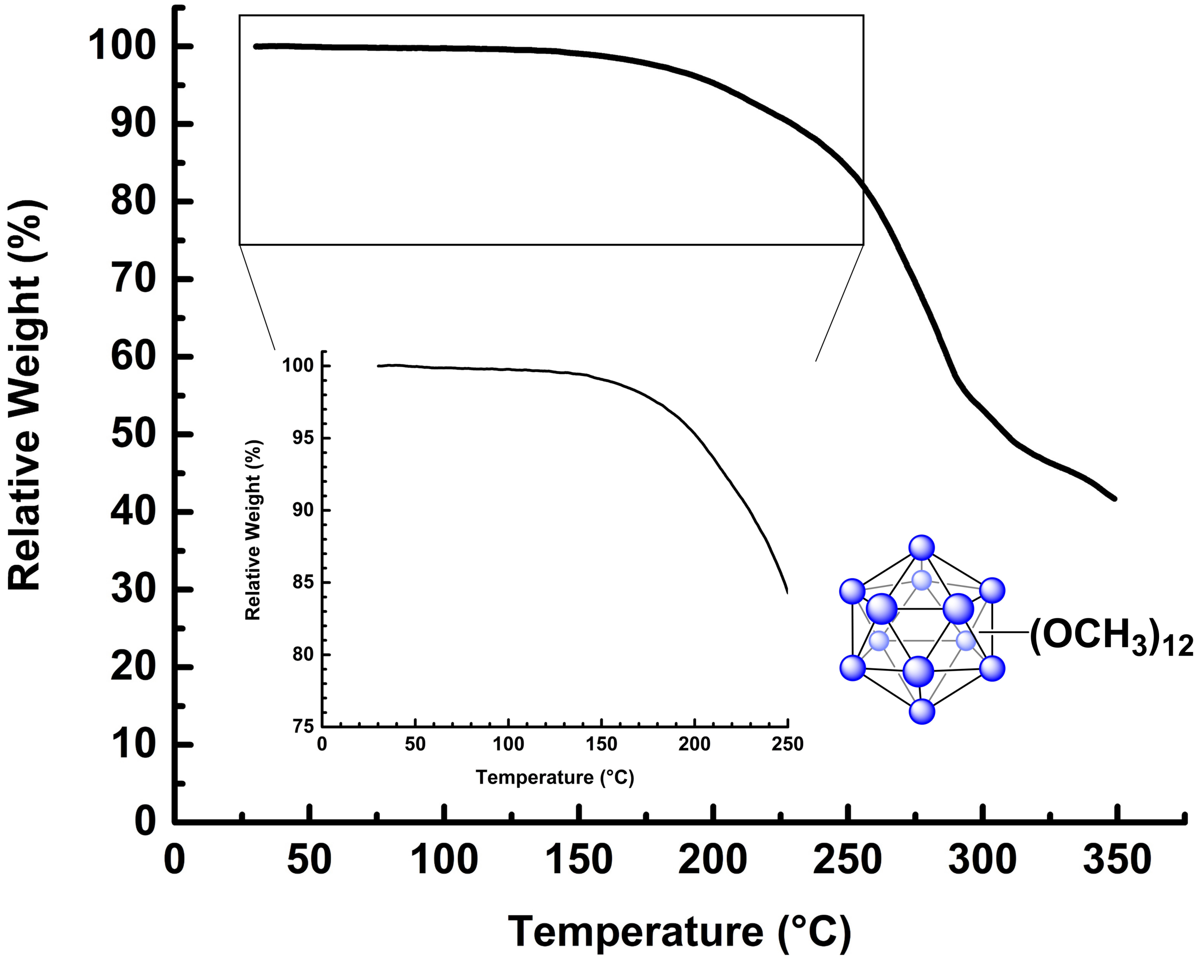

Figure S8. TGA of a powder sample of $B_{12}(OCH_3)_{12}$.

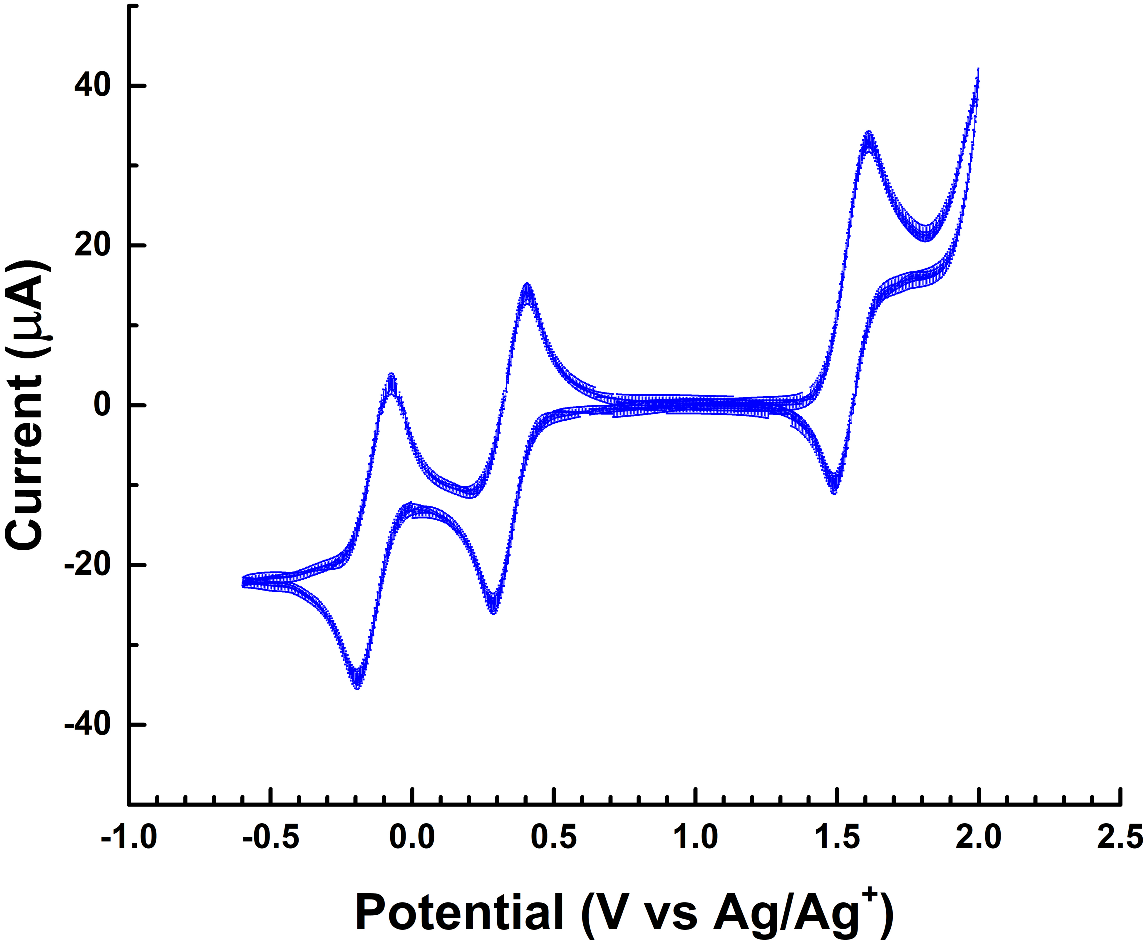

Figure S9. Raw, unsmoothed cyclic voltammogram of $B_{12}(OCH_3)_{12}$ in DCM.

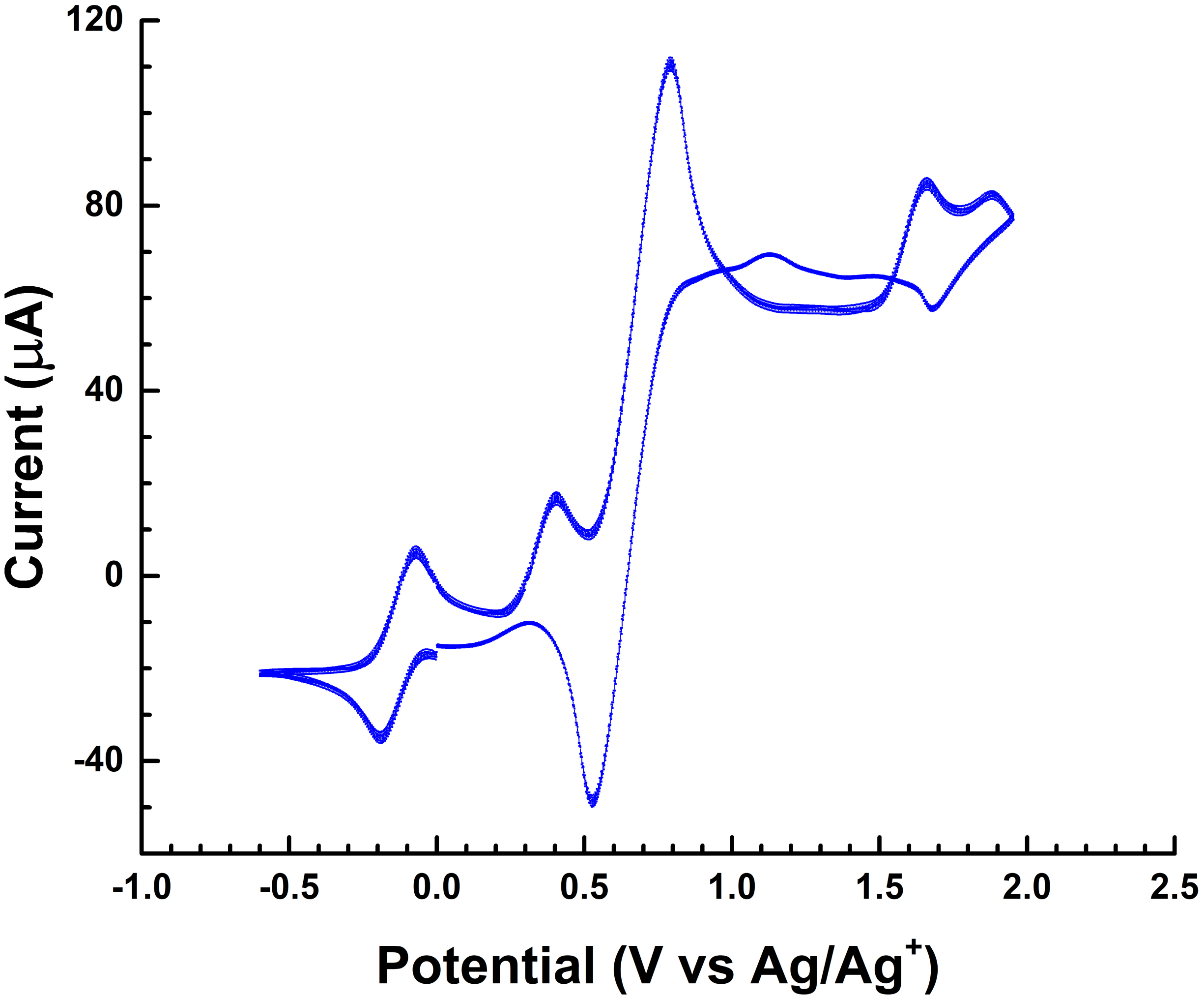

Figure S10. Raw, unsmoothed cyclic voltammogram of $B_{12}(OCH_3)_{12}$ with ferrocene internal standard in DCM.

IV. Characterization of $Li_2[B_{12}(OCH_3)_{12}]$

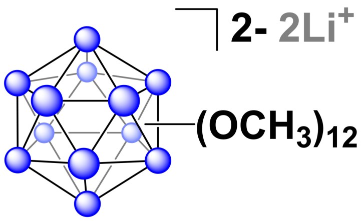

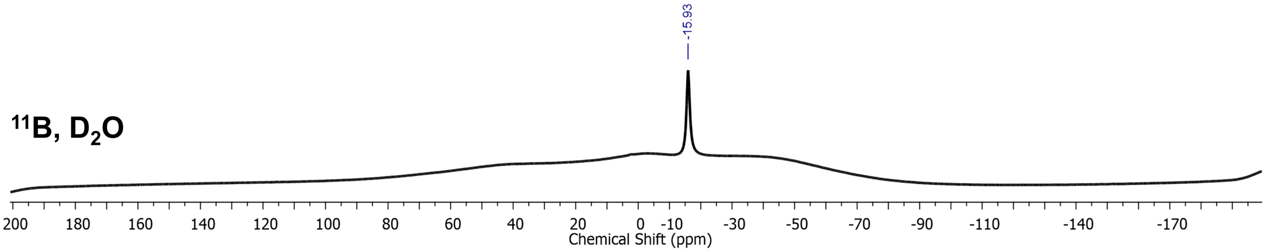

Figure S11. ^{11}B NMR spectrum of $Li_2[B_{12}(OCH_3)_{12}]$ in D_2O.

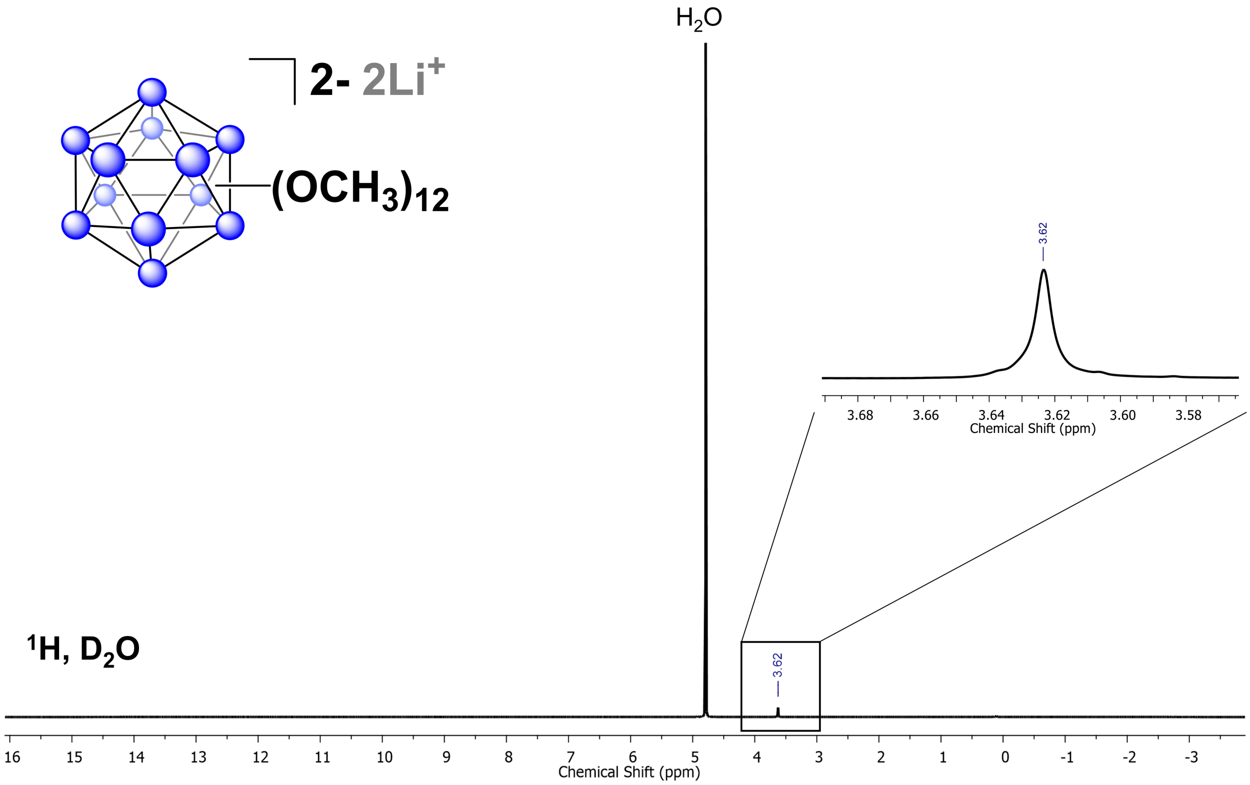

Figure S12. ^{1}H NMR spectrum of $Li_2[B_{12}(OCH_3)_{12}]$ in D_2O.

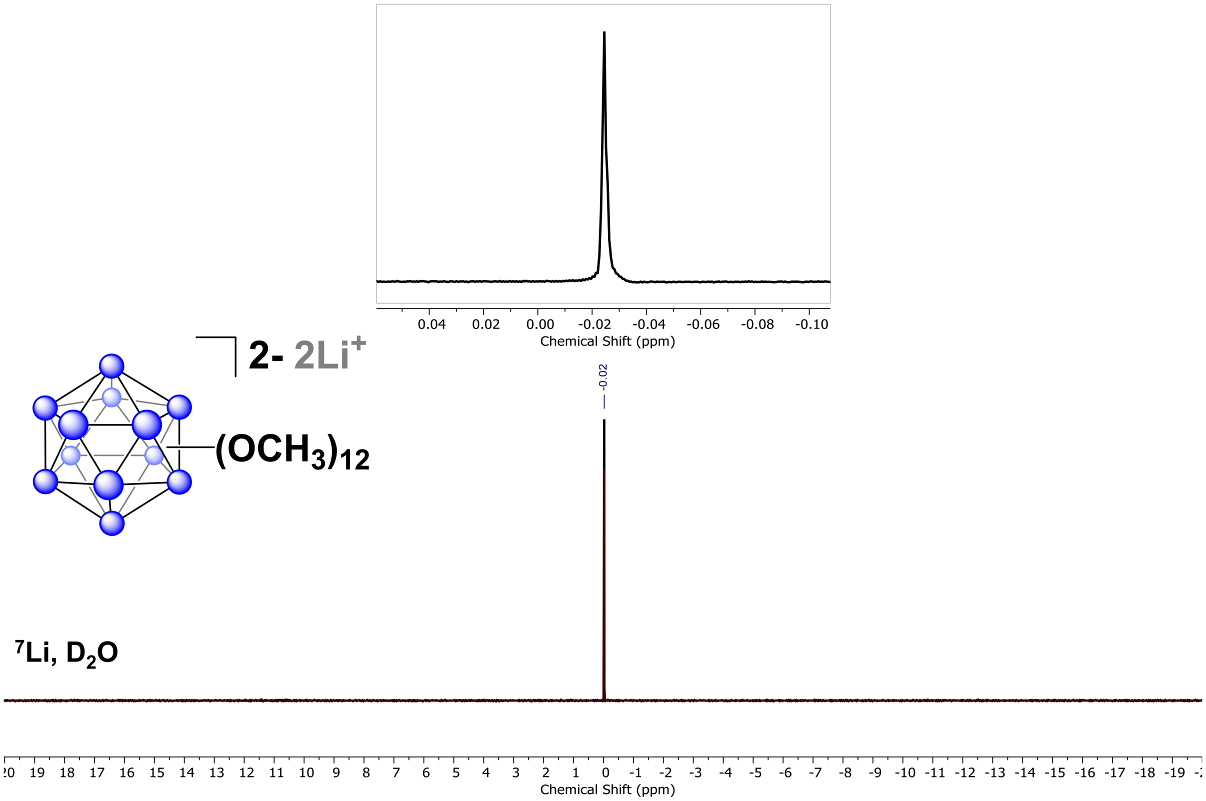

Figure S13. ^{7}Li NMR spectrum of $Li_2[B_{12}(OCH_3)_{12}]$ in D_2O.

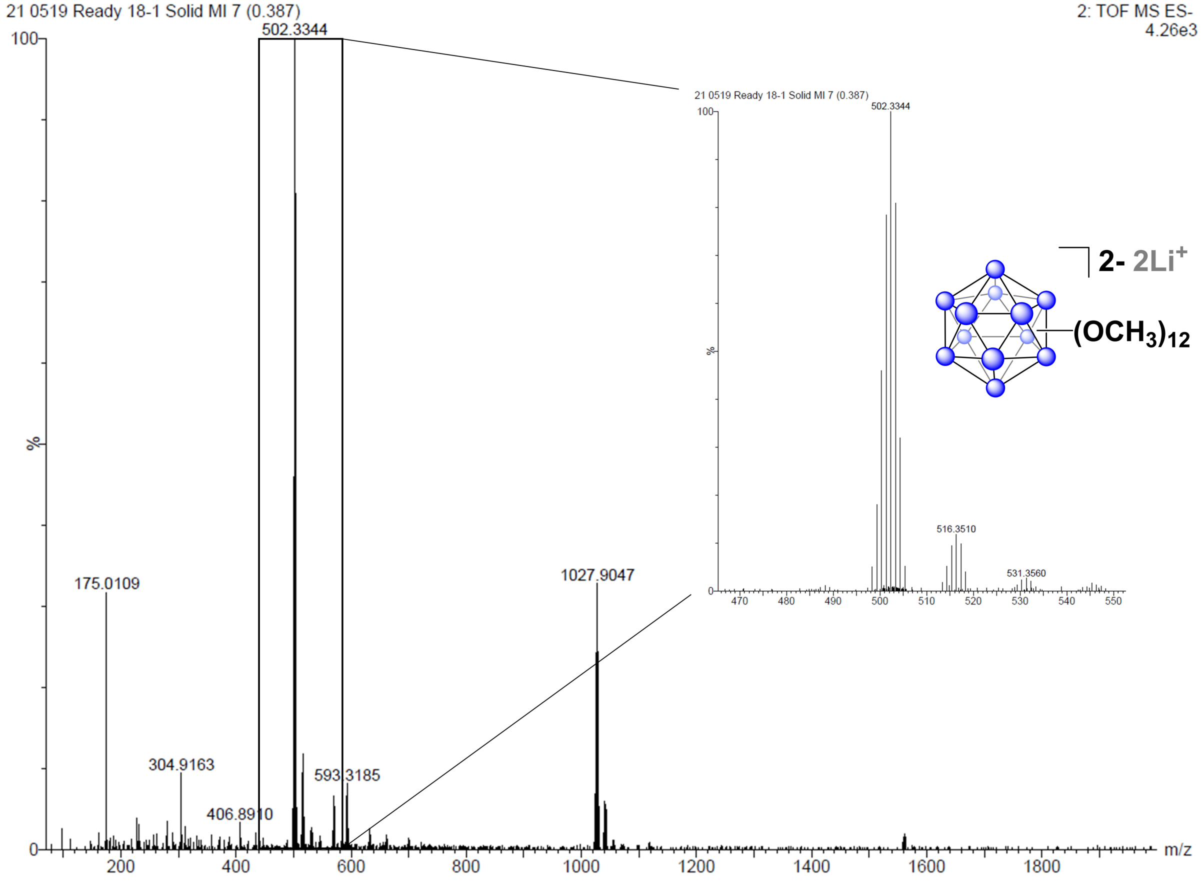

Figure S14. Full mass spectrum of $Li_2[B_{12}(OCH_3)_{12}]$ in H_2O. Electrospray ionization, negative mode; observed as $[M]^-$.

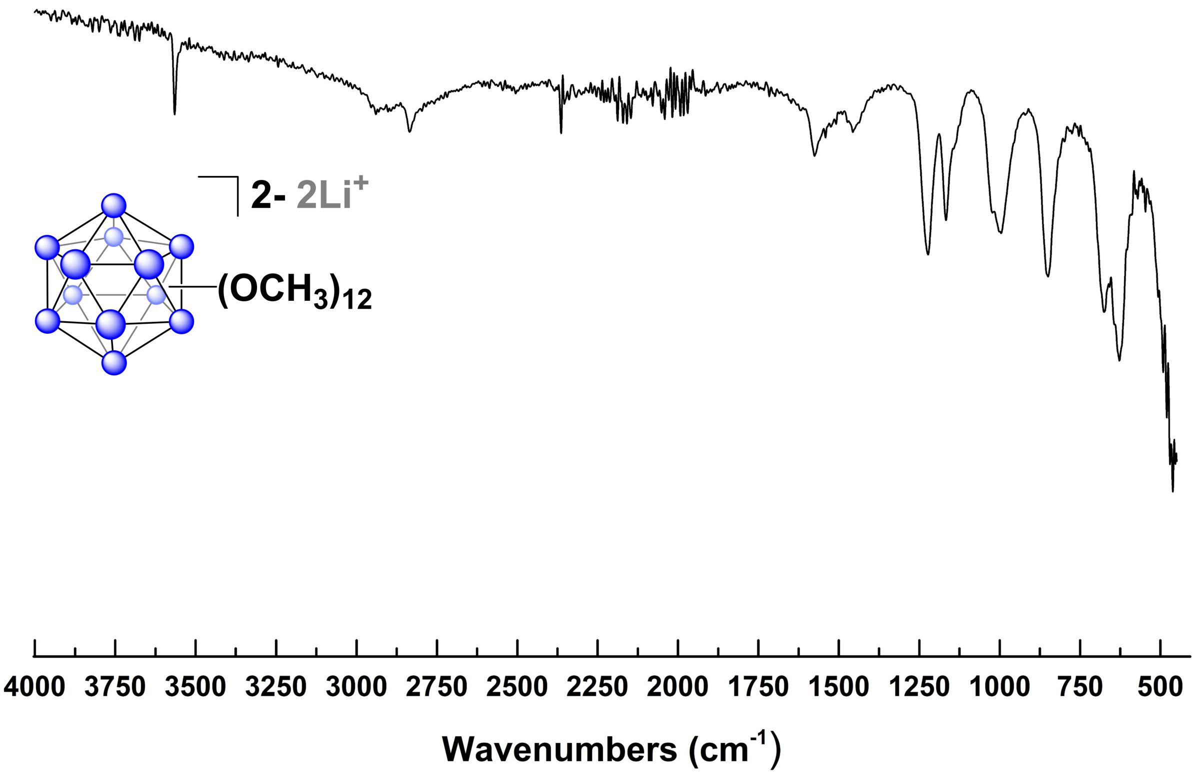

Figure S15. FTIR of a powder sample of $Li_2[B_{12}(OCH_3)_{12}]$.

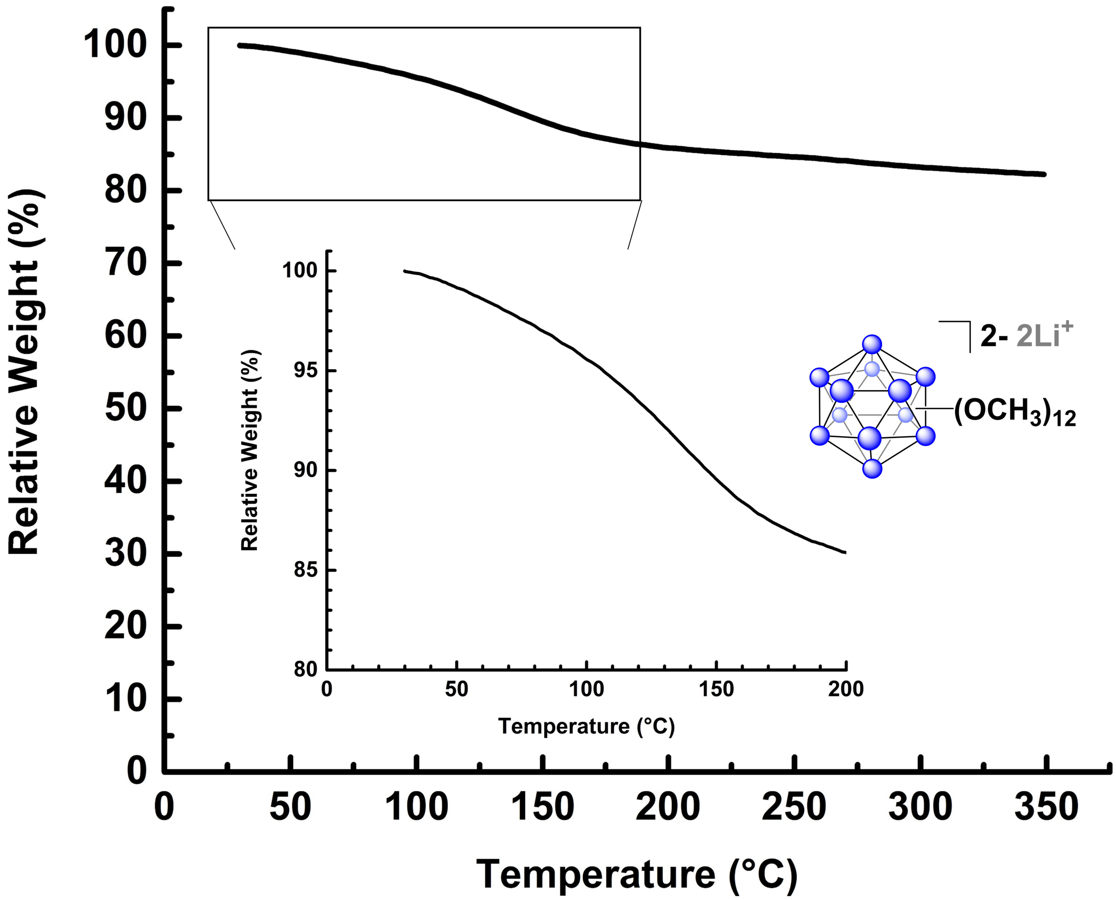

Figure S16. TGA of a powder sample of $Li_2[B_{12}(OCH_3)_{12}]$.

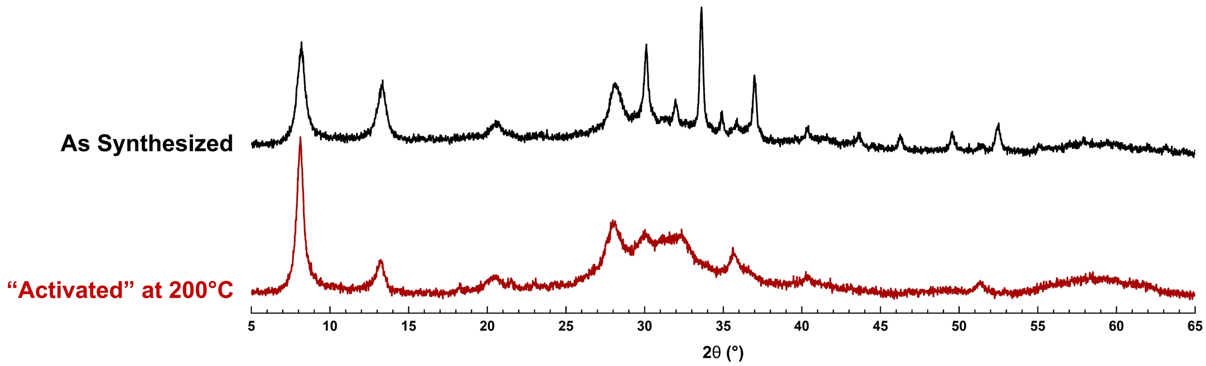

Figure S17. PXRD of "As Synthesized" and thermally "Activated" samples of $Li_2[B_{12}(OCH_3)_{12}]$. Activation was achieved by heating the parent compound at 200°C in vacuo for 12 hours.

V. XPS Data

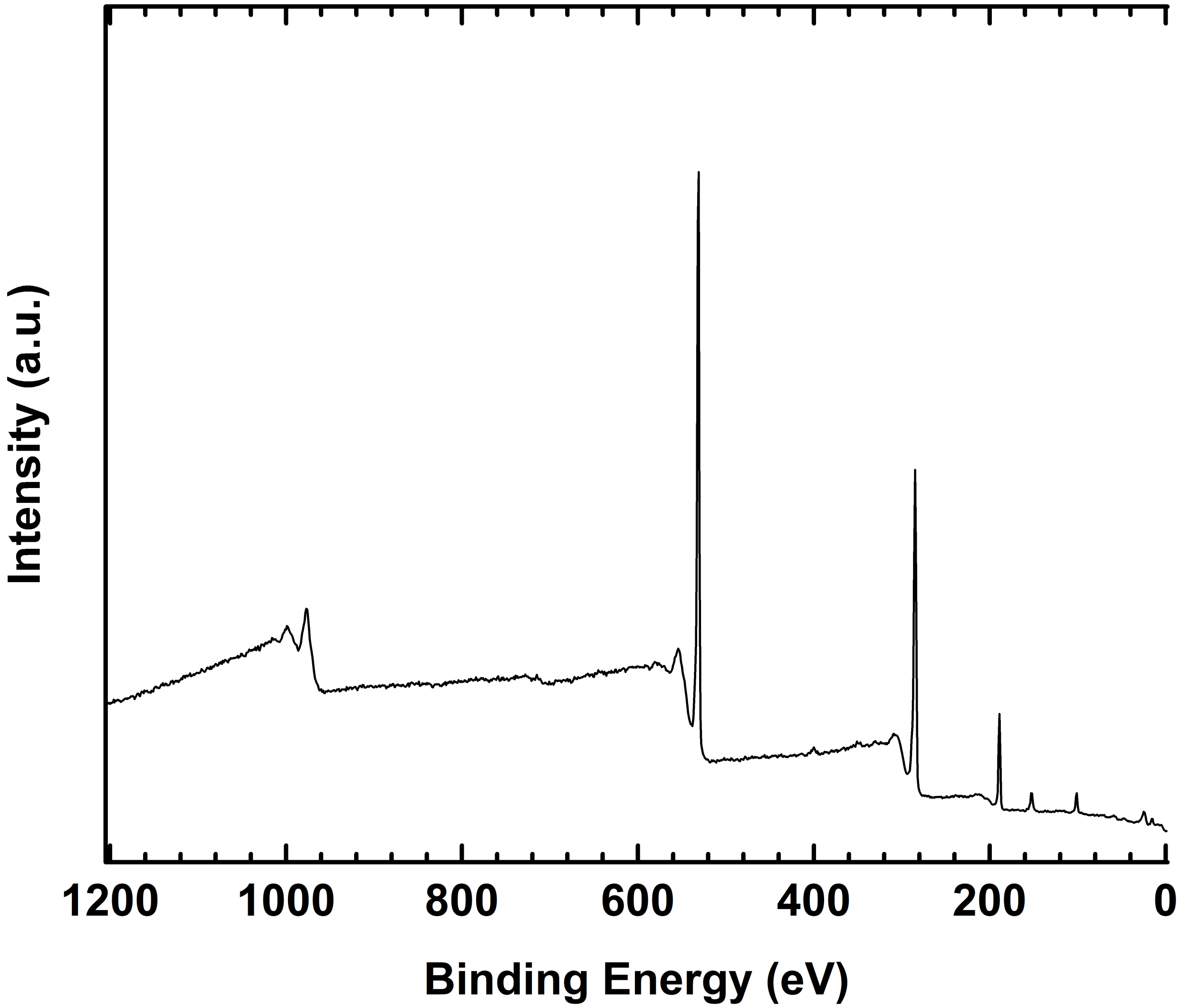

Figure S18. Full spectrum XPS survey of a powder sample of $[B_{12}(OCH_3)_{12}]^0$. Note the absence of any signals corresponding to Ce 3d electrons (880 - 920 eV).

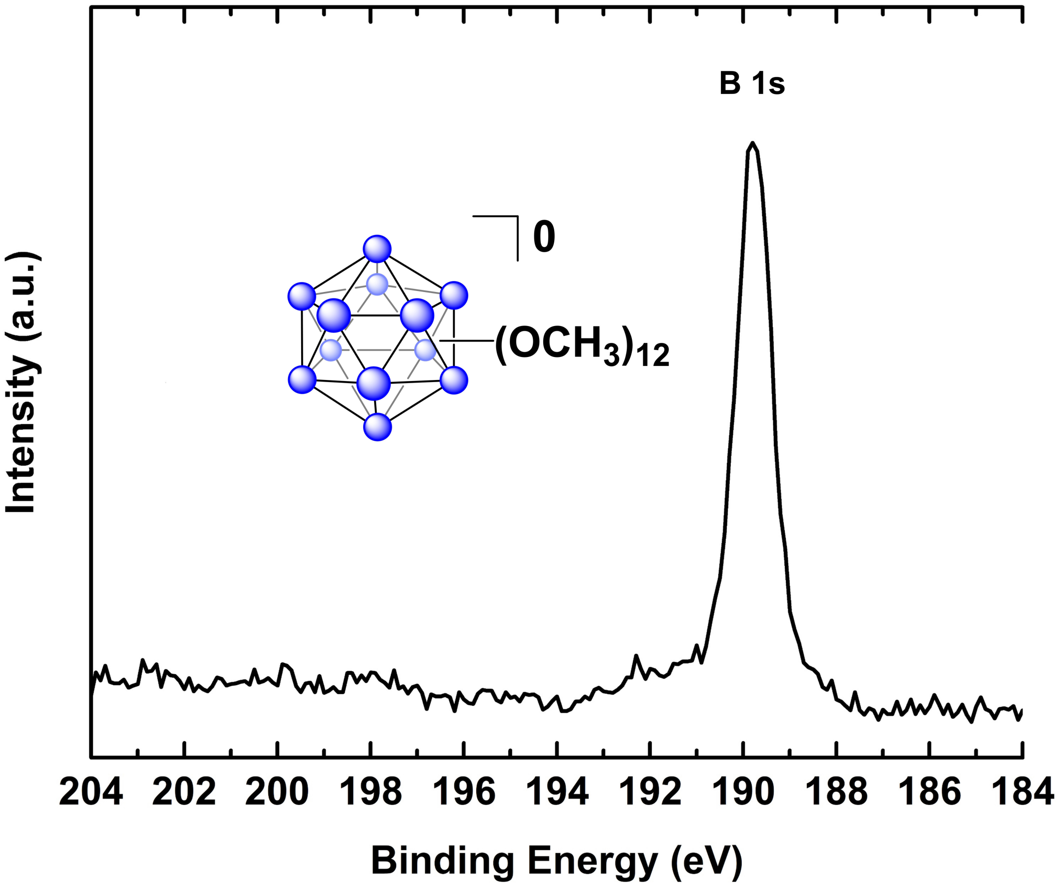

Figure S19. XPS of the boron 1s region of a powder sample of $[B_{12}(OCH_3)_{12}]^0$.

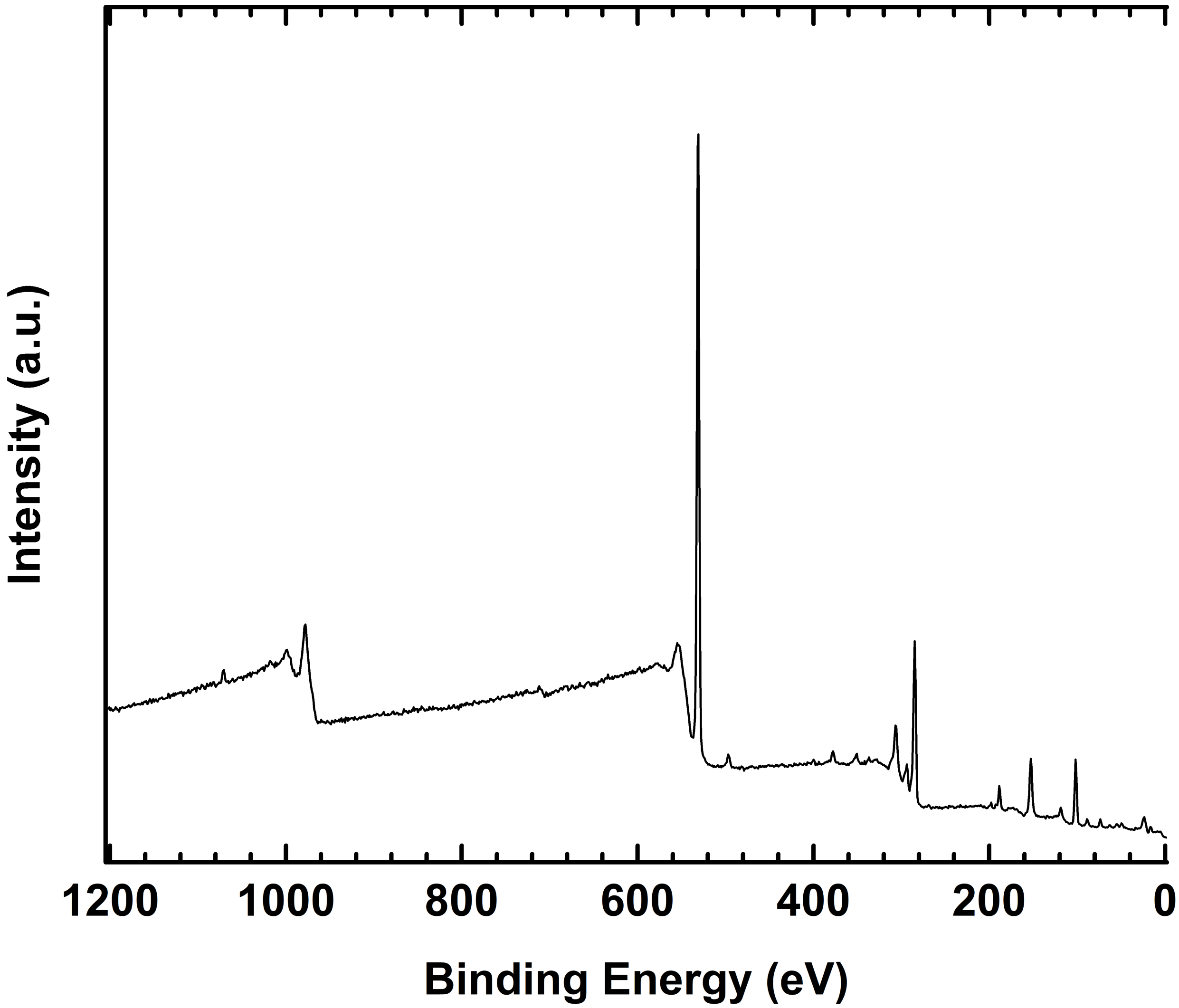

Figure S20. Full spectrum XPS survey of a powder sample of $Li_2[B_{12}(OCH_3)_{12}]$.

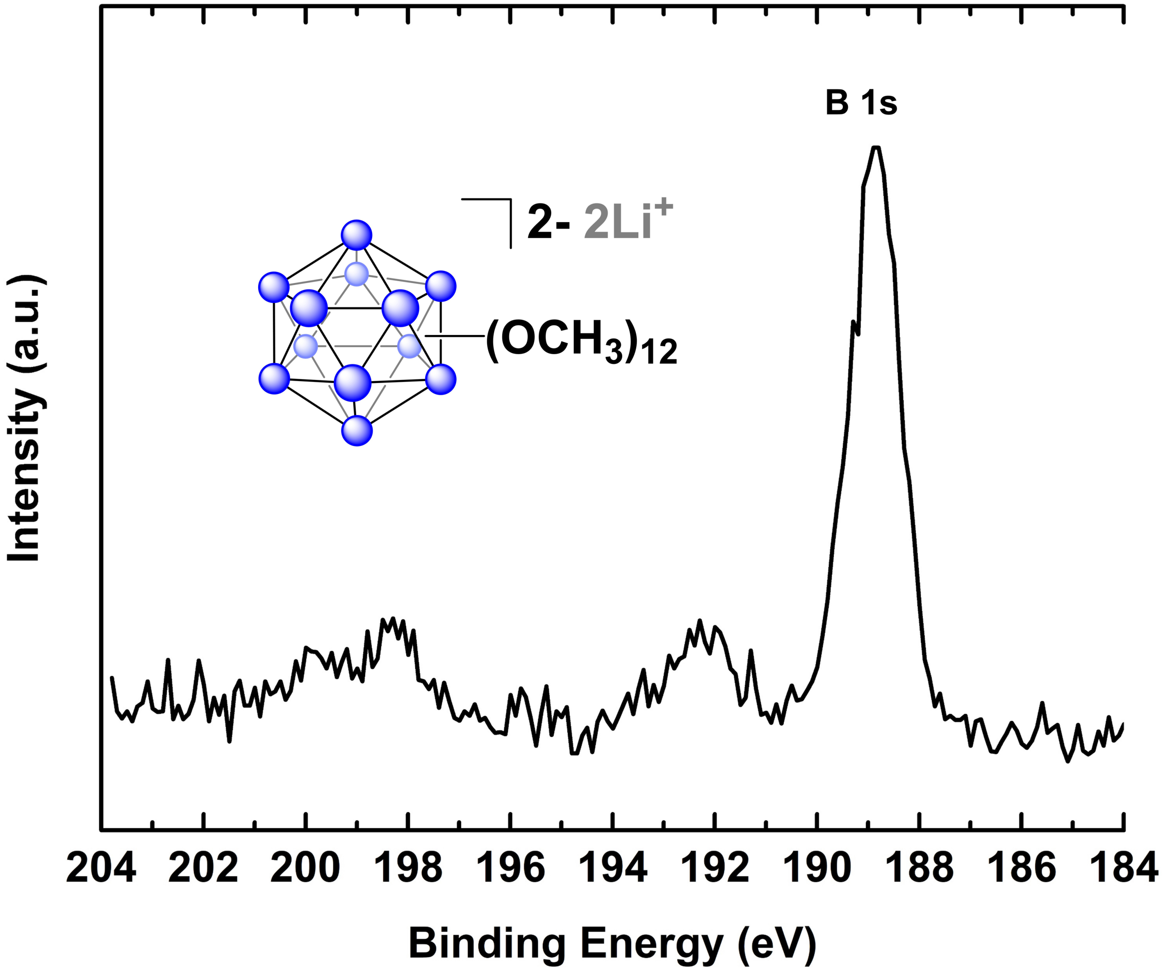

Figure S21. XPS of the boron 1s region of a powder sample of $Li_2[B_{12}(OCH_3)_{12}]$.

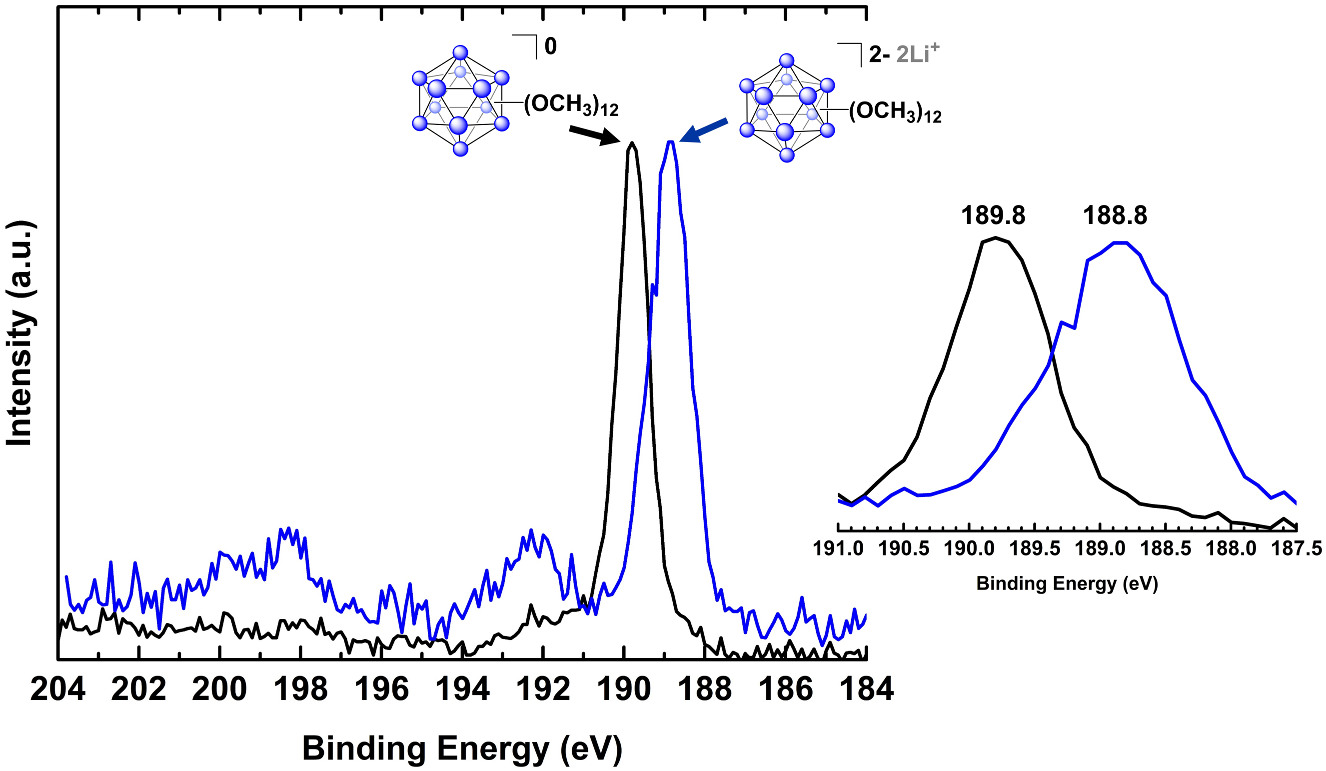

Figure S22. Comparison of XPS data for the boron 1s region of $[B_{12}(OCH_3)_{12}]^0$ and $Li_2[B_{12}(OCH_3)_{12}]$, with zoomed inset.

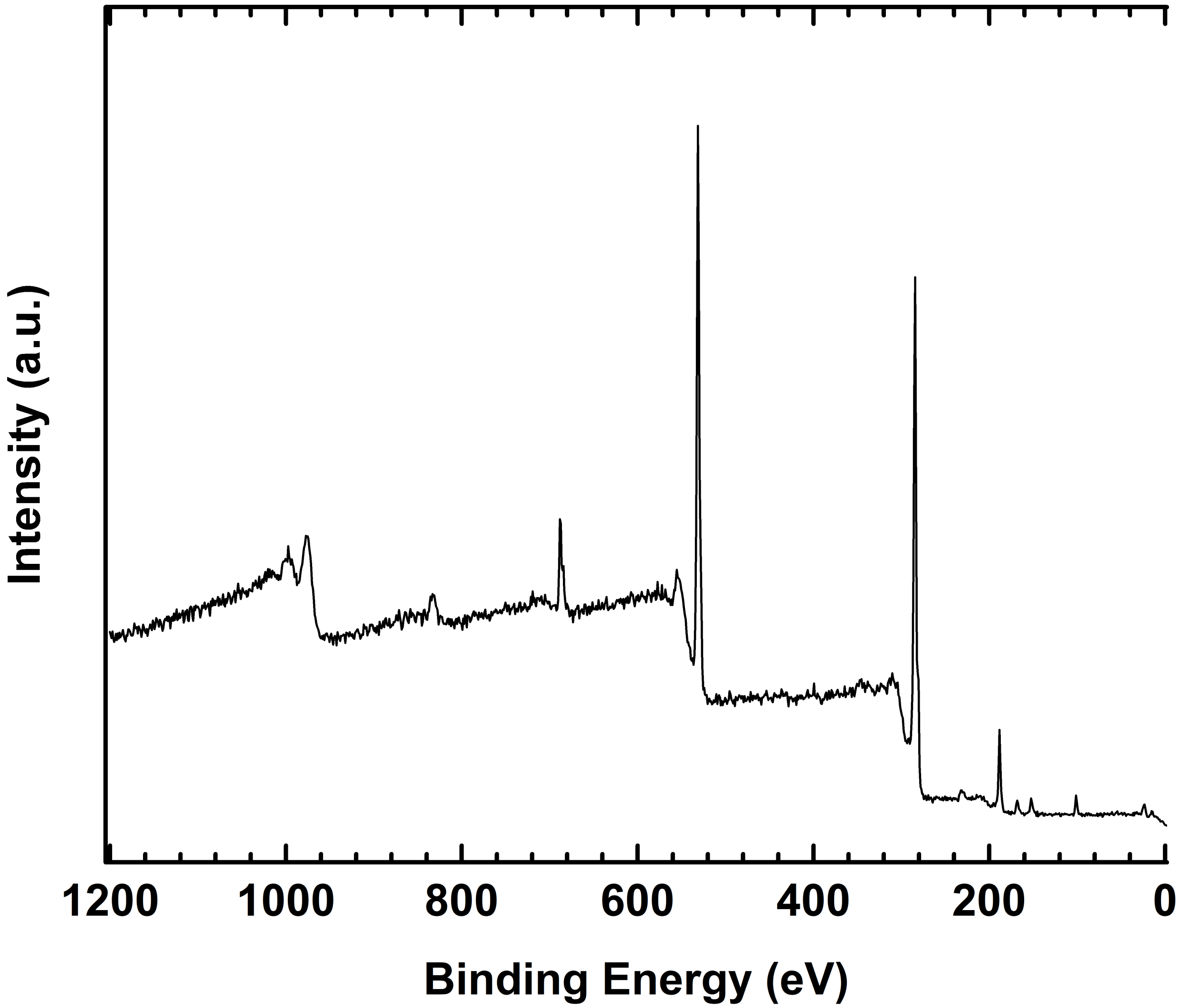

Figure S23. Full spectrum XPS survey of a fully discharged electrochemical cell containing $[B_{12}(OCH_3)_{12}]^0$. Small peaks attributed to fluorine 1s and sulfur 2p electrons originate from the presence of LiTFSI in the cell.

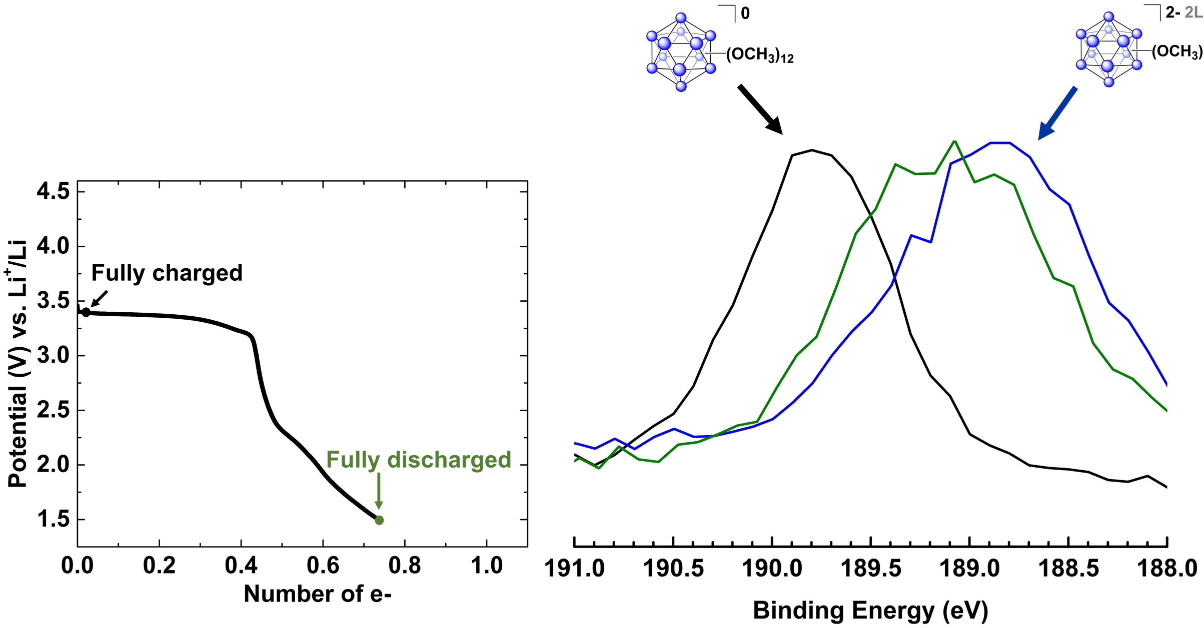

Figure S24. XPS data for the boron 1s region of a fully discharged electrochemical cell containing $[B_{12}(OCH_3)_{12}]^0$, as compared to independently synthesized samples of $[B_{12}(OCH_3)_{12}]^0$ and $Li_2[B_{12}(OCH_3)_{12}]$.

VI. Electrochemical Cycling of $B_{12}(OCH_3)_{12}$ and $Li_2[B_{12}(OCH_3)_{12}]$

Materials and Methods:

Polyethylene oxide (PEO, Aldrich, MW 600,000), aluminum oxide (Al_2O_3, Aldrich, 99.9%, <1.0 Micron), SuperP® (Alfa Aesar), lithium bis(trifluoromethanesulfonyl)imide (LiTFSI, Aldrich) and tetrahydrofuran (THF, HPLC > 99.9%) were used as received. Lithium disks (MTI, 99.9%, 16 mm diameter and 0.6 mm thick) were polished prior to cell assembly. The as-prepared boron clusters with molecular formulas $B_{12}(OCH_3)_{12}$ and $Li_2[B_{12}(OCH_3)_{12}]$ were pre-dried in a vacuum oven at 110°C for 4 h and 200°C for 12 h, respectively. To prepare the electrode, PEO and LiTFSI were dissolved in an 8:1 molar ratio in THF at 55°C with constant stirring. To this clear solution, SuperP® and the boron cluster were added. The weight ratio of active boron cluster, PEO-LiTFSI, and SuperP® was 60:20:20. The solution was coated onto aluminum foil using a doctor blade for a thickness of 10 µm and dried under dynamic vacuum overnight. The electrode was then punched into 16 mm diameter disks. The PEO-Al_2O_3-LiTFSI solid polymer electrolyte (PEO-SPE) layer was prepared by dissolving PEO and LiTFSI in an 8:1 molar ratio in THF at 55°C, to which 10 wt% Al_2O_3 was added with stirring. The solution was coated on to lithium and dried in vacuo overnight. The all-solid-state boron cluster/PEO-SPE/Li full cell was constructed by pressing the boron-containing electrode directly on to the PEO-SPE coated lithium electrode, and then sealed in coin cells (Type CR-2032) with stainless steel positive and negative cases, spacers, and spring (all from MTI). Electrode preparation and cell assembly was done in an Ar-filled glove box ($[H_2O] < 1$ ppm and $[O_2] < 1$ ppm).

All cells were equilibrated for 3 h at 60°C prior to electrochemical testing, which was also conducted at 60°C. Cyclic voltammograms were recorded at 0.1 mVs^{-1} in the potential range of 1.50 - 4.15 V vs Li/Li^+, with the first scan in the cathodic or anodic directions for $B_{12}(OCH_3)_{12}$ and $Li_2[B_{12}(OCH_3)_{12}]$, respectively. The galvanostatic (dis)charge measurements were carried out at a C/20 rate in the potential range of 1.50 - 4.15 V vs. Li^+/Li. Electrochemical impedance spectroscopy (EIS) measurements were made at different depths of discharge (DOD) in the frequency range of 100 kHz - 0.1 Hz at 10 mV sinusoidal excitation. The cells were discharged at C/20 rate in steps of 5 % DOD and allowed to relax for 30 minutes. The EIS spectra were then recorded at this stable open circuit potential. The resulting impedance data was analyzed with ZSimpWin software using an equivalent circuit model.

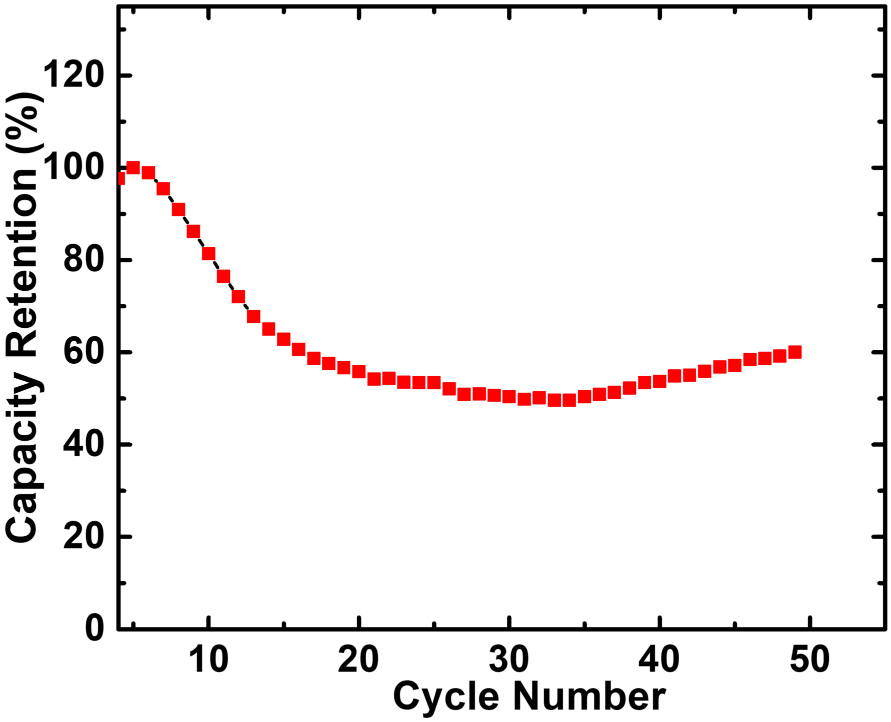

Figure S25. Capacity retention of a $B_{12}(OCH_3)_{12}$/PEO-SPE/Li cell over 50 cycles at C/2 rate. The cycling was carried out at 60°C.

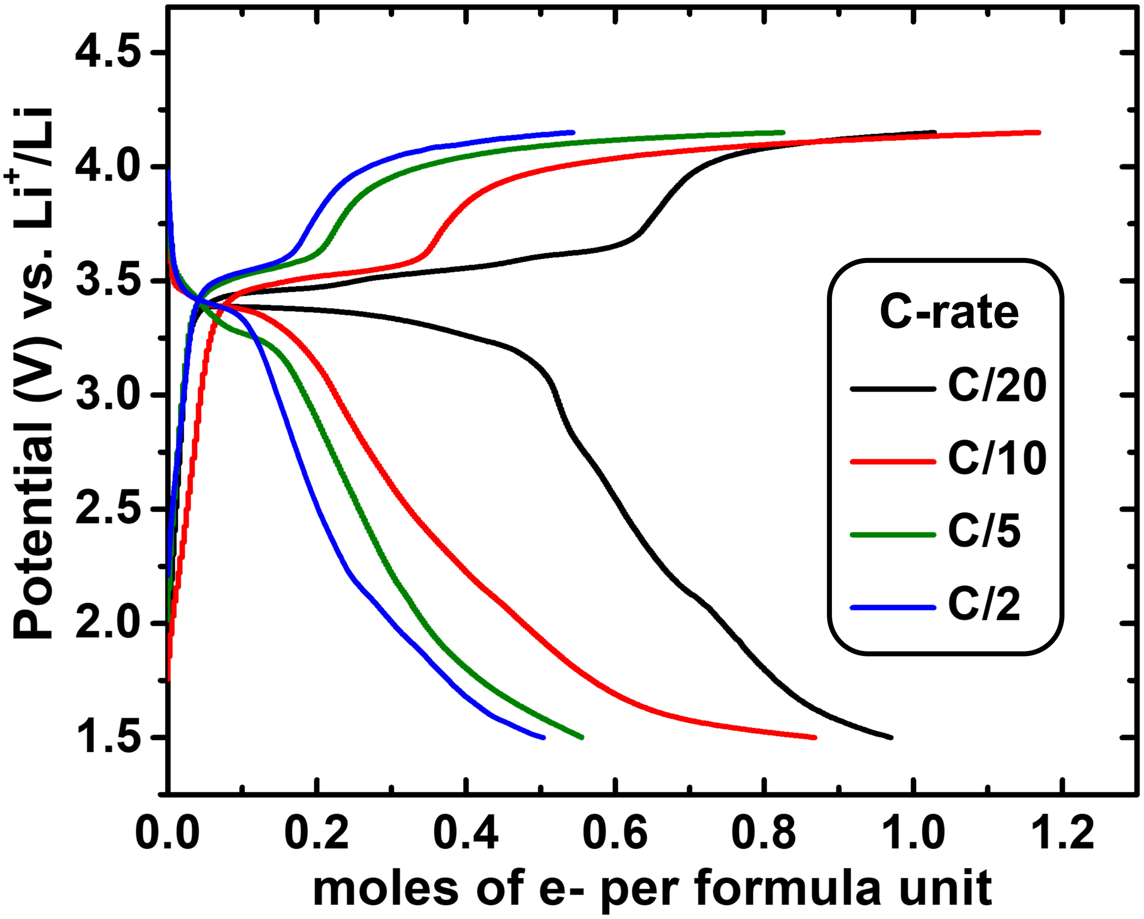

Figure S26. Charge-discharge curves of $B_{12}(OCH_3)_{12}$/PEO-SPE/Li cells at different C-rates. All measurements were performed at 60°C.

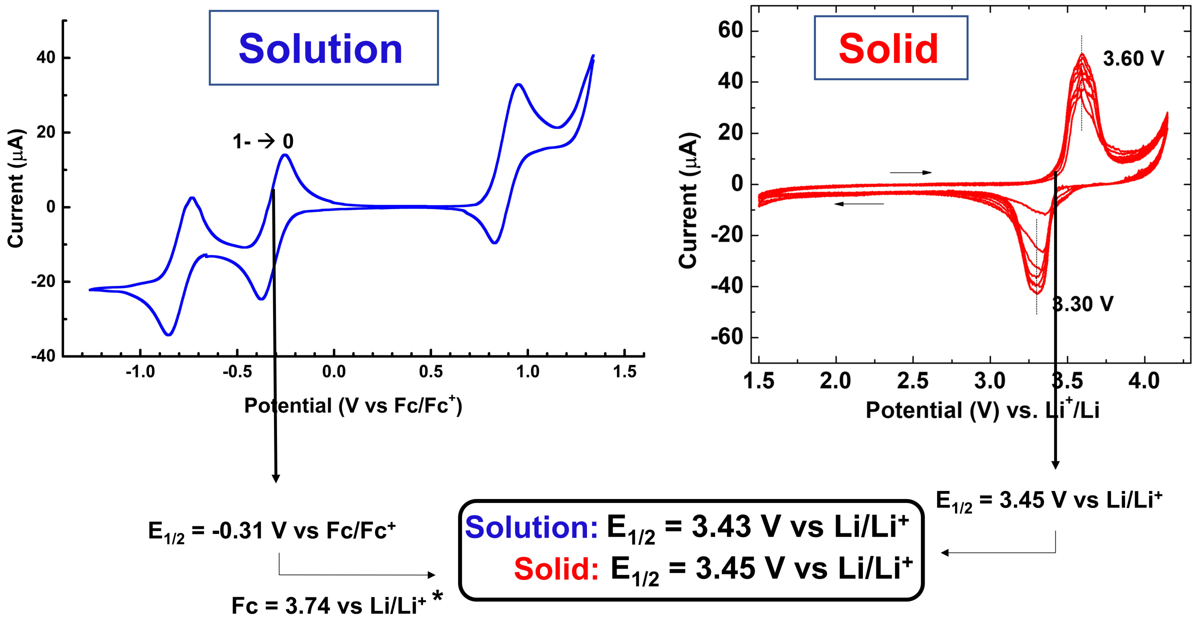

Figure S27. Comparison of the $[B_{12}(OCH_3)_{12}]^{1-}$/ $[B_{12}(OCH_3)_{12}]^{0}$ redox couple ([TBA]PF_6, DCM, vs Fc/Fc^+) to the observed redox couple in a solid state electrochemical cell (LiTFSI, vs Li/Li^+).

*Calculated using:

Fc/Fc^+ = 0.46 V vs SCE (0.1 M TBA[PF_6] in DCM)[5]

Li/Li^+ = -3.04 V vs SHE[6]

SCE = 0.24 V vs SHE[7]

In order to compare the electrochemical activity of $Li_2[B_{12}(OCH_3)_{12}]$ with $B_{12}(OCH_3)_{12}$, cyclic voltammetry and galvanostatic cycling were repeated for a $Li_2[B_{12}(OCH_3)_{12}]$ /PEO-SPE/Li cell. For CV measurements, the potential was scanned from its open circuit potential (OCP) of 2.6 V to 4.15 V, and then back to 1.5 V. During the first anodic sweep, a broad oxidation peak appeared around 3.6 V, however, a reduction peak with significantly diminished current was observed in the cathodic sweep, indicating poor reversibility of the boron cluster redox (Figure S25A). A similar trend was also observed during galvanostatic cycling (Figure S25B). Although the cell could be charged to its full capacity, an extremely low active material utilization corresponding to only 0.15 e^- transfer was obtained during discharge, consistent with the CV data.

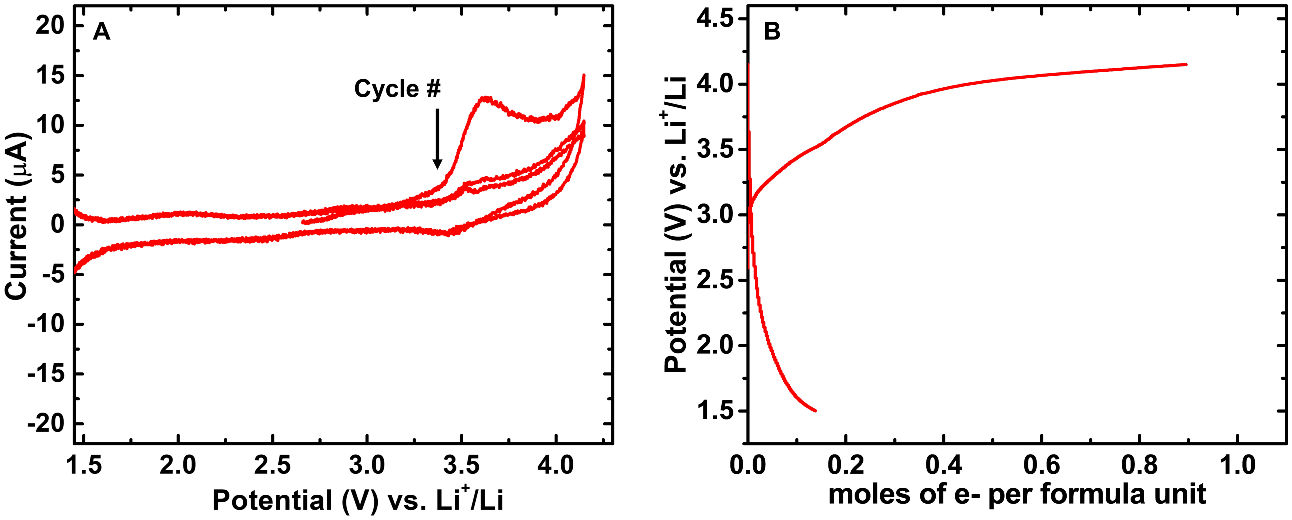

Figure S28. (A) Cyclic voltammetry of a $Li_2[B_{12}(OCH_3)_{12}]$/PEO-SPE/Li cell at 0.1 mV s^{-1}. (B) Galvanostatic cycling at a C/20 rate. All measurements were performed at 60°C.

VII. Single Crystal X-ray Diffraction of $B_{12}(OCH_3)_{12}$

The single crystal X-ray diffraction studies were carried out on a Bruker APEX II Ultra CCD diffractometer equipped with Mo K_α radiation ($\lambda = 0.71073$). Crystals of the subject compound were used as received, grown from evaporation of a dichloromethane solution. A 0.130 x 0.110 x 0.080 mm red block crystal was mounted on a Cryoloop with Paratone oil. Data were collected in a nitrogen gas stream at 100(2) K using ϕ and ϖ scans. Crystal-to-detector distance was 40 mm using exposure time 15.0 second with a scan width of 0.70°. Data collection was 99.9% complete to 25.242° in θ. A total of 4816 reflections were collected covering the indices, $-19 \leq h \leq 18$, $-16 \leq k \leq 19$, $-12 \leq l \leq 12$. 943 reflections were found to be symmetry independent, with a R_{int} of 0.0644. Indexing and unit cell refinement indicated a Trigonal lattice. The space group was found to be *R*-3. The data were integrated using the Bruker SAINT Software program and scaled using the SADABS software program. Solution by direct methods (SHELXT) produced a complete phasing model consistent with the proposed structure.

All nonhydrogen atoms were refined anisotropically by full-matrix least-squares (SHELXL-2014). All carbon bonded hydrogen atoms were placed using a riding model. Their positions were constrained relative to their parent atom using the appropriate HFIX command in SHELXL-2014. Due to the intrinsic symmetry of this compound, a “total” disorder in an approximate ratio of 85/15 was fitted. SAME and ISOR instruction has been used to constrain the minority fragment.

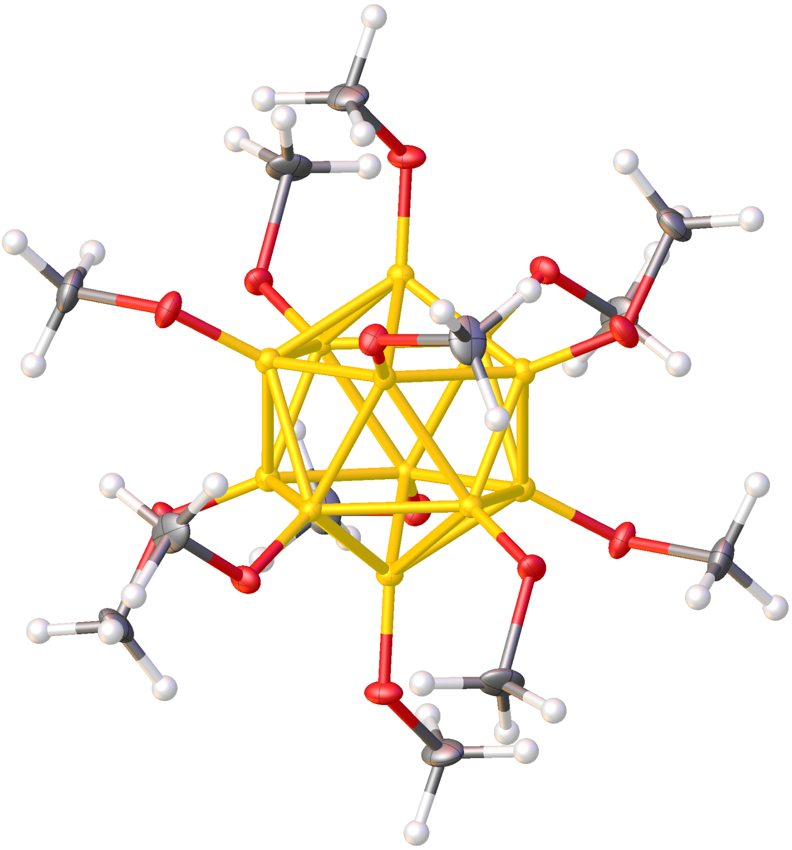

Figure S29. Single crystal structure of $B_{12}(OCH_3)_{12}$. Non-hydrogen atoms shown as 50% probability ellipsoids; hydrogens depicted as spheres.

Table S1. Crystal data and structure refinement for $B_{12}(OCH_3)_{12}$.

Empirical formula	C12 H36 B12 O12	
Molecular formula	C12 H36 B12 O12	
Formula weight	502.13	
Temperature	100.0 K	
Wavelength	0.71073 Å	
Crystal system	Trigonal	
Space group	R -3	
Unit cell dimensions	a = 14.8343(11) Å	α= 90°.
	b = 14.8343(11) Å	β= 90°.
	c = 9.7274(15) Å	γ = 120°.
Volume	1853.8(4) Å^3	
Z	3	
Density (calculated)	1.349 Mg/m^3	
Absorption coefficient	0.102 mm^{-1}	
F(000)	792	
Crystal size	0.13 x 0.11 x 0.08 mm^3	
Crystal color, habit	Red Block	
Theta range for data collection	2.626 to 27.474°.	
Index ranges	-19<=h<=18, -16<=k<=19, -12<=l<=12	
Reflections collected	4816	
Independent reflections	943 [R(int) = 0.0644]	
Completeness to theta = 25.242°	99.9 %	

Absorption correction	Semi-empirical from equivalents
Max. and min. transmission	0.4862 and 0.4011
Refinement method	Full-matrix least-squares on F^2
Data / restraints / parameters	943 / 33 / 114
Goodness-of-fit on F^2	1.073
Final R indices [I>2sigma(I)]	R1 = 0.0429, wR2 = 0.1129
R indices (all data)	R1 = 0.0541, wR2 = 0.1202
Largest diff. peak and hole	0.339 and -0.225 e.Å^{-3}

Table S2. Atomic coordinates (x 10^4) and equivalent isotropic displacement parameters (Å^{2}x 10^3) for $B_{12}(OCH_3)_{12}$. U(eq) is defined as one third of the trace of the orthogonalized U^{ij} tensor.

	x	y	z	U(eq)
O(1)	3589(1)	5517(1)	4115(1)	12(1)
O(2)	5484(1)	6855(1)	5958(1)	14(1)
C(1)	2735(3)	4807(3)	3303(3)	22(1)
C(2)	6398(2)	7442(3)	6747(5)	21(1)
B(1)	3464(1)	6018(1)	5248(2)	9(1)
B(2)	4538(1)	6780(1)	6284(2)	10(1)
O(1')	4805(5)	7132(5)	4126(6)	15(2)
O(2')	4266(5)	5237(4)	5960(6)	13(2)
C(1')	4965(19)	7870(20)	3100(20)	42(8)
C(2')	3848(17)	4215(9)	6500(30)	28(6)
B(1')	4148(7)	6935(6)	5248(8)	8(2)
B(2')	3846(6)	5865(5)	6284(8)	8(2)

Table S3. Bond lengths [Å] and angles [°] for $B_{12}(OCH_3)_{12}$.

O(1)-C(1)	1.415(3)	O(2')-C(2')	1.420(7)
O(1)-B(1)	1.3933(18)	O(2')-B(2')	1.392(5)
O(2)-C(2)	1.416(4)	C(1')-H(1'A)	0.9800
O(2)-B(2)	1.3871(19)	C(1')-H(1'B)	0.9800
C(1)-H(1A)	0.9800	C(1')-H(1'C)	0.9800
C(1)-H(1B)	0.9800	C(2')-H(2'A)	0.9800
C(1)-H(1C)	0.9800	C(2')-H(2'B)	0.9800
C(2)-H(2A)	0.9800	C(2')-H(2'C)	0.9800
C(2)-H(2B)	0.9800	B(1')-B(1')#1	1.847(14)
C(2)-H(2C)	0.9800	B(1')-B(1')#2	1.847(15)
B(1)-B(1)#1	1.857(3)	B(1')-B(2')	1.738(5)
B(1)-B(1)#2	1.857(3)	B(1')-B(2')#4	1.866(12)
B(1)-B(2)	1.741(2)	B(1')-B(2')#1	1.859(12)
B(1)-B(2)#3	1.867(2)	B(2')-B(2')#3	1.857(8)
B(1)-B(2)#2	1.868(2)	B(2')-B(2')#4	1.857(8)
B(2)-B(2)#3	1.865(2)		
B(2)-B(2)#4	1.865(2)	B(1)-O(1)-C(1)	122.01(15)
O(1')-C(1')	1.413(6)	B(2)-O(2)-C(2)	122.97(16)
O(1')-B(1')	1.393(5)	O(1)-C(1)-H(1A)	109.5

O(1)-C(1)-H(1B)	109.5
O(1)-C(1)-H(1C)	109.5
H(1A)-C(1)-H(1B)	109.5
H(1A)-C(1)-H(1C)	109.5
H(1B)-C(1)-H(1C)	109.5
O(2)-C(2)-H(2A)	109.5
O(2)-C(2)-H(2B)	109.5
O(2)-C(2)-H(2C)	109.5
H(2A)-C(2)-H(2B)	109.5
H(2A)-C(2)-H(2C)	109.5
H(2B)-C(2)-H(2C)	109.5
O(1)-B(1)-B(1)#1	121.31(10)
O(1)-B(1)-B(1)#2	122.64(10)
O(1)-B(1)-B(2)	118.77(13)
O(1)-B(1)-B(2)#2	123.35(12)
O(1)-B(1)-B(2)#3	122.42(12)
B(1)#2-B(1)-B(1)#1	60.002(1)
B(1)#1-B(1)-B(2)#2	105.12(9)
B(1)#2-B(1)-B(2)#3	105.12(8)
B(1)#1-B(1)-B(2)#3	109.07(7)
B(1)#2-B(1)-B(2)#2	55.74(10)
B(2)-B(1)-B(1)#2	110.51(9)
B(2)-B(1)-B(1)#1	62.45(10)
B(2)-B(1)-B(2)#2	110.24(13)
B(2)-B(1)-B(2)#3	62.12(7)
B(2)#3-B(1)-B(2)#2	59.91(6)
O(2)-B(2)-B(1)#4	123.29(12)
O(2)-B(2)-B(1)	118.73(13)
O(2)-B(2)-B(1)#1	122.08(12)
O(2)-B(2)-B(2)#4	123.24(12)
O(2)-B(2)-B(2)#3	121.78(12)
B(1)-B(2)-B(1)#4	110.22(13)
B(1)#4-B(2)-B(1)#1	104.88(12)
B(1)-B(2)-B(1)#1	61.80(12)
B(1)-B(2)-B(2)#3	62.26(8)
B(1)-B(2)-B(2)#4	110.11(8)
B(2)#4-B(2)-B(1)#4	55.62(10)
B(2)#3-B(2)-B(1)#1	108.69(7)
B(2)#4-B(2)-B(1)#1	60.03(8)
B(2)#3-B(2)-B(1)#4	60.06(10)
B(2)#3-B(2)-B(2)#4	105.13(11)
B(1')-O(1')-C(1')	122.9(9)
B(2')-O(2')-C(2')	121.9(9)
O(1')-C(1')-H(1'A)	109.5
O(1')-C(1')-H(1'B)	109.5
O(1')-C(1')-H(1'C)	109.5

H(1'A)-C(1')-H(1'B)	109.5	B(2')-B(1')-B(2')#4	61.9(3)
H(1'A)-C(1')-H(1'C)	109.5	B(2')#1-B(1')-B(2')#4	59.8(3)
H(1'B)-C(1')-H(1'C)	109.5	O(2')-B(2')-B(1')	118.8(5)
O(2')-C(2')-H(2'A)	109.5	O(2')-B(2')-B(1')#3	123.1(6)
O(2')-C(2')-H(2'B)	109.5	O(2')-B(2')-B(2')#3	123.1(6)
O(2')-C(2')-H(2'C)	109.5	O(2')-B(2')-B(2')#4	121.9(7)
H(2'A)-C(2')-H(2'B)	109.5	B(1')-B(2')-B(1')#3	110.3(5)
H(2'A)-C(2')-H(2'C)	109.5	B(1')#2-B(2')-B(1')#3	105.2(5)
H(2'B)-C(2')-H(2'C)	109.5	B(1')-B(2')-B(2')#4	62.4(4)
O(1')-B(1')-B(2')	118.7(5)	B(1')-B(2')-B(2')#3	110.2(3)
O(1')-B(1')-B(2')#4	121.8(7)	B(2')#4-B(2')-B(1')#3	59.9(5)
B(1')#1-B(1')-B(2')#4	105.2(3)	B(2')#3-B(2')-B(1')#3	55.7(4)
B(1')#2-B(1')-B(2')#4	108.9(4)	B(2')#3-B(2')-B(2')#4	105.0(5)

Symmetry transformations used to generate equivalent atoms:

#1 -y+1,x-y+1,z   #2 -x+y,-x+1,z   #3 y-1/3,-x+y+1/3,-z+4/3

#4 x-y+2/3,x+1/3,-z+4/3

Table S4. Anisotropic displacement parameters ($Å^2 x 10^3$) for $B_{12}(OCH_3)_{12}$. The anisotropic displacement factor exponent takes the form: $-2\pi^2[h^2 a^{*2}U^{11} + ... + 2 h k a^* b^* U^{12}]$

	U^{11}	U^{22}	U^{33}	U^{23}	U^{13}	U^{12}
O(1)	12(1)	14(1)	11(1)	-4(1)	-2(1)	7(1)
O(2)	9(1)	21(1)	12(1)	-3(1)	-1(1)	9(1)
C(1)	21(1)	21(1)	16(1)	-13(1)	-3(1)	6(1)
C(2)	9(1)	26(2)	26(2)	-5(1)	-3(1)	8(1)
B(1)	8(1)	9(1)	9(1)	0(1)	0(1)	4(1)
B(2)	10(1)	11(1)	9(1)	1(1)	0(1)	6(1)
O(1')	20(3)	14(3)	14(3)	3(2)	3(2)	11(3)
O(2')	16(3)	11(3)	16(3)	4(2)	4(3)	8(3)
C(1')	45(12)	45(10)	52(11)	24(7)	6(7)	33(8)
C(2')	36(10)	38(9)	25(8)	5(6)	-3(7)	30(7)
B(1')	7(3)	10(4)	8(3)	2(3)	1(3)	5(3)
B(2')	7(3)	5(3)	10(4)	0(3)	-3(3)	1(3)

Table S5. Hydrogen coordinates (x 10^4) and isotropic displacement parameters (Å^{2}x 10 ^{3}) for $B_{12}(OCH_3)_{12}$.

	x	y	z	U(eq)
H(1A)	2985	4547	2554	33
H(1B)	2383	5160	2919	33
H(1C)	2246	4222	3876	33
H(2A)	6938	7293	6437	31
H(2B)	6244	7255	7720	31
H(2C)	6644	8186	6631	31
H(1'A)	4565	7517	2280	64
H(1'B)	5707	8273	2873	64
H(1'C)	4735	8347	3448	64
H(2'A)	4418	4095	6756	42
H(2'B)	3414	3707	5798	42
H(2'C)	3424	4139	7310	42

VIII. Rietveld Refinement of $B_{12}(OCH_3)_{12}$ from Powder Diffraction Data

The information about lattice parameters and space group used in the reconstruction of $B_{12}(OCH_3)_{12}$ from experimental PXRD data was obtained from the single crystal structure. The shape of the boron cluster was fixed as a rigid body and a simulated annealing approach implemented in TOPAS was used to find boron cluster positions, as well as the positions of oxygen and carbon atoms. We attempted to pinpoint the hydrogen atoms with the Difference Fourier map, but unfortunately this approach was not successful. Therefore, hydrogen atoms were omitted from further calculations, which caused a noticeable underestimation of the intensities of some peaks (Figure S26). Lastly, a Rietveld refinement was performed in order to precisely determine the lattice parameters, atom positions, and the quality of the fit (Table S1-S3).

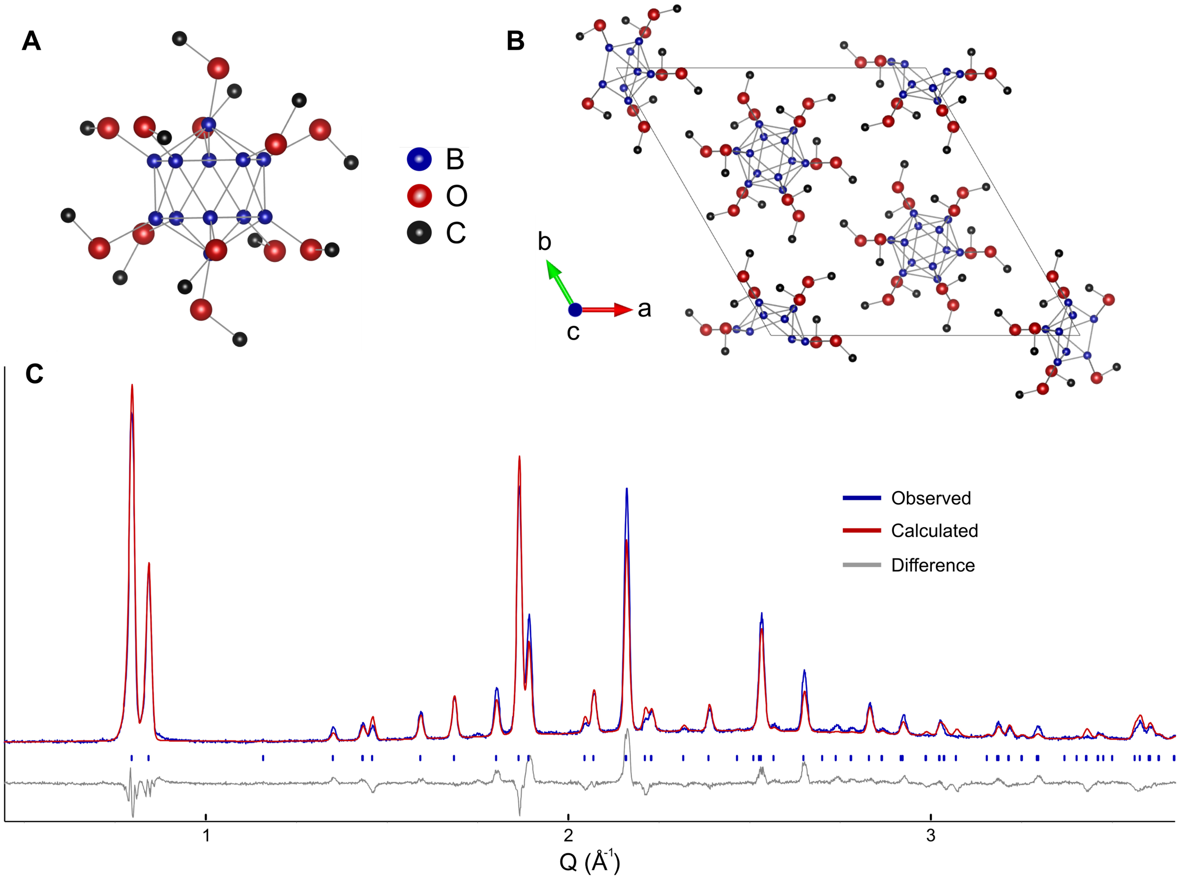

Figure S30. (A) Structure of constructed boron cluster for refinement (hydrogens omitted) (B) Structure of rhombohedral unit cell (C) Rietveld refinement of experimental powder diffraction pattern of $B_{12}(OCH_3)_{12}$.

Lattice Parameters		
Parameter (Ǻ)	**Single Crystal**	**Powder Refinement**
a	14.8343 (11)	14.9242 (4)
c	9.7274 (15)	9.9767 (4)

Table S6. Comparison of the lattice parameters for $B_{12}(OCH_3)_{12}$ as determined from both the single crystal structure and refinement of the powder pattern.

Powder Refinement			
Atom Positions	**x**	**y**	**z**
Site B1	0.1225	0.09948	-0.032525
Site B2	0.07521	0.06111	0.135495
Site O1	0.2164 (4)	0.1942 (7)	-0.0690 (6)
Site O2	0.1442 (6)	0.1222 (5)	0.2732 (7)
Site C1	0.3094 (6)	0.2271 (7)	-0.0031 (7)
Site C2	0.1362 (8)	0.1964 (6)	0.3194 (9)

Table S7. Atomic positions of all atoms (excluding hydrogens) in $B_{12}(OCH_3)_{12}$ as determined via refinement of the powder pattern.

Reliability Factors	
R_{wp}	8.67
GOF	3.18

Table S8. Reliability factors for Rietveld refinement of $B_{12}(OCH_3)_{12}$ powder pattern.

Cell Composition	**% Utilization**	**Coulombic Efficiency (%)**	**Rate, Temp (°C)**	**Reference**
S/PEO-Al_2O_3/Li	85	63 (11th cycle)	C/10, 60	J. Electroanal. Chem., 2021, 881, 114916
LFP/PEO-Al_2O_3/Li	90	~99	C/10, 60	Electrochim. Acta, 2023, 437, 14150
LCO/PEO-Al_2O_3/Li	52 (142 mAh g^{-1})	99.7	C/2, 60	Energy Storage Mater., 32 (2020) 191
LFP/PEO-LTP/Li	76	>95	C/5, 80	J. Phys. Chem. C, 2018, 122, 9852
LCO/PEO/Li	43 (120 mAh g^{-1})	<90	C/10, 60	Adv. Funct. Mater., 2020, 30, 1909392
LFP/PEO-$Li_{21}Si_5$/ Li	76	~100	C/10, 60	Adv. Mater., 2021, 33, 2004711
$B_{12}(OCH_3)_{12}$/PEO-Al_2O_3/Li	**95**	**96**	**C/20, 60**	**This Work**

Table S9. Literature comparison of the performance of PEO-based all-solid-state cells.

Analysis of Synchrotron Data of $Li_2[B_{12}(OCH_3)_{12}]$

The qualitative phase analysis was assessed using HighScore Plus software, with implemented ICSD database.

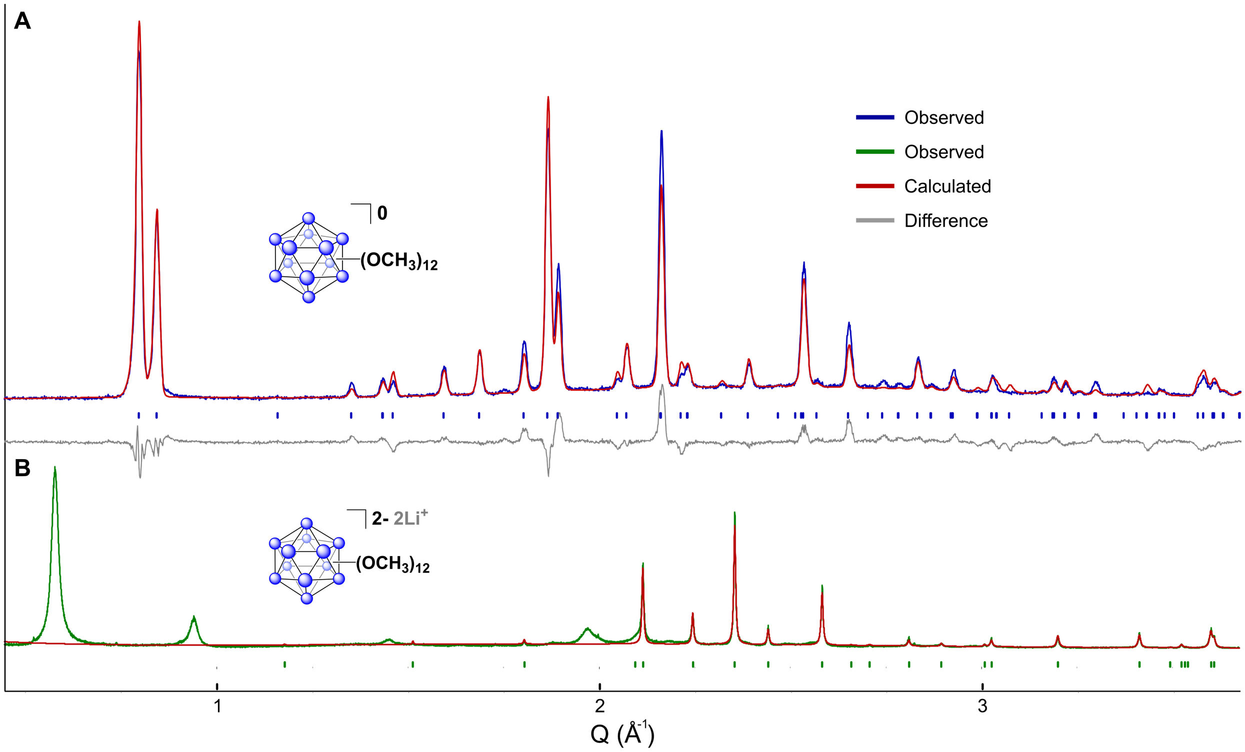

Figure S31. (A) Rietveld refinement of experimental powder diffraction pattern of $B_{12}(OCH_3)_{12}$. (B) Synchrotron diffraction pattern of $Li_2[B_{12}(OCH_3)_{12}]$ (green line) with admixture of $LiOH{\cdot}H_2O$ impurity (green tick marks).

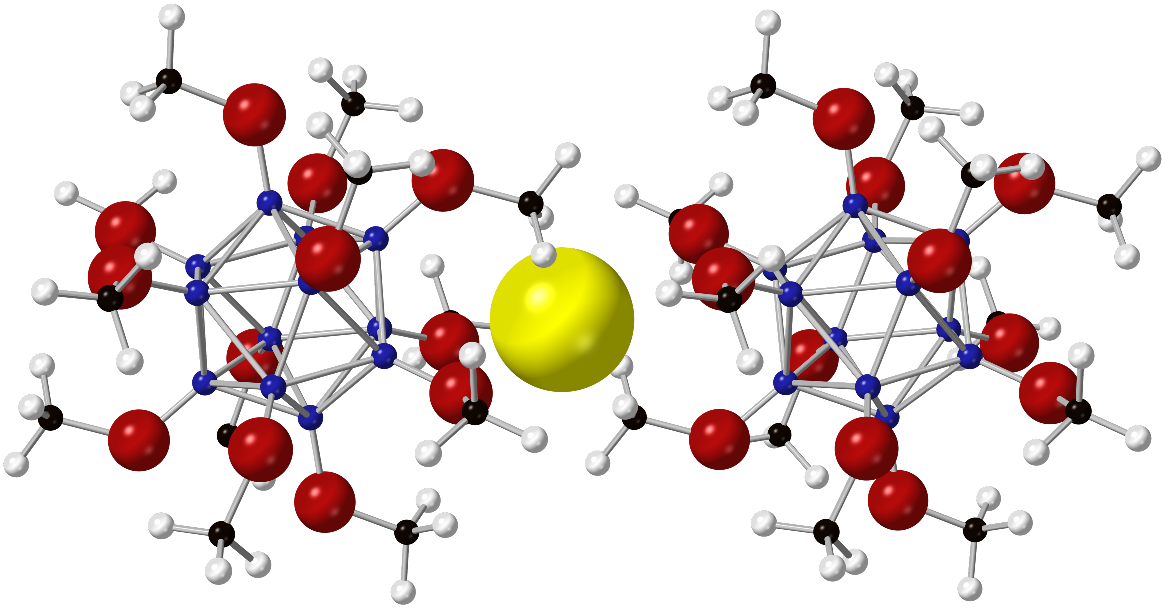

Figure S32. Visualization of a 2.8 Å cavity (yellow sphere) between -OCH$_3$ moieties on neighboring $B_{12}(OCH_3)_{12}$ clusters; simulated via CrystalMaker from the single crystal structure of $B_{12}(OCH_3)_{12}$.

REFERENCES

(1) Farha, O. K.; Julius, R. L.; Lee, M. W., et al., Synthesis of Stable Dodecaalkoxy Derivatives of hypercloso-$B_{12}H_{12}$. *J. Am. Chem. Soc.,* **2005,** *127* (51), 18243-18251.

(2) Wixtrom, A. I.; Shao, Y.; Jung, D., et al., Rapid synthesis of redox-active dodecaborane $B_{12}(OR)_{12}$ clusters under ambient conditions. *Inorg. Chem. Front.,* **2016,** *3* (5), 711-717.

(3) Wixtrom, A. I.; Parvez, Z. A.; Savage, M. D., et al., Tuning the electrochemical potential of perfunctionalized dodecaborate clusters through vertex differentiation. *Chem. Commun.,* **2018,** *54* (46), 5867-5870.

(4) McKee, M. L., Density Functional Theory Study of Anionic and Neutral Per-Substituted 12-Vertex Boron Cage Systems, $B_{12}X_{12}^{n-}$ (n = 2, 1, 0). *Inorg. Chem.,* **2002,** *41* (5), 1299-1305.

(5) Connelly, N. G.; Geiger, W. E., Chemical Redox Agents for Organometallic Chemistry. *Chem. Rev.,* **1996,** *96* (2), 877-910.

(6) Haynes, W. M. *CRC Handbook of Chemistry and Physics*. CRC Press, 2014.

(7) Sawyer, D. T.; Sobkowiak, A.; Roberts, J. L. *Electrochemistry for Chemists*. Wiley-Interscience, 1995.